Aus dem Zentrum für Innere Medizin der Universität zu Köln
Klinik und Poliklinik für Innere Medizin I
Direktor: Universitätsprofessor Dr. med. Michael Hallek

Deciphering the role of NEDD9-dependant signaling cascades in the pathophysiology of clear-cell renal cell carcinoma

Inaugural-Dissertation zur Erlangung der Doktorwürde
der Medizinischen Fakultät
der Universität zu Köln

vorgelegt von
Denise Biermann
aus Köln

promoviert am 29. November 2024

Gedruckt mit Genehmigung der Medizinischen Fakultät der Universität zu Köln

Druckjahr 2025

Dekan: Universitätsprofessor Dr. med. G. R. Fink
1. Gutachter: Universitätsprofessor Dr. med. C. P. Pallasch
2. Gutachterin: Universitätsprofessorin PhD C. M. Niessen

Erklärung

Ich erkläre hiermit, dass ich die vorliegende Dissertationsschrift ohne unzulässige Hilfe Dritter und ohne Benutzung anderer als der angegebenen Hilfsmittel angefertigt habe; die aus fremden Quellen direkt oder indirekt übernommenen Gedanken sind als solche kenntlich gemacht.

Bei der Auswahl und Auswertung des Materials sowie bei der Herstellung des Manuskriptes habe ich Unterstützungsleistungen von folgenden Personen erhalten: Frau Dr. med. Tamina Seeger-Nukpezah und Frau Dr. Nelly Mikhael.

Weitere Personen waren an der Erstellung der vorliegenden Arbeit nicht beteiligt. Insbesondere habe ich nicht die Hilfe einer Promotionsberaterin/eines Promotionsberaters in Anspruch genommen. Dritte haben von mir weder unmittelbar noch mittelbar geldwerte Leistungen für Arbeiten erhalten, die im Zusammenhang mit dem Inhalt der vorgelegten Dissertationsschrift stehen.

Die Dissertationsschrift wurde von mir bisher weder im Inland noch im Ausland in gleicher oder ähnlicher Form einer anderen Prüfungsbehörde vorgelegt.

Die in dieser Arbeit von mir ausgewerteten histologischen Schnitte aus Tierversuchen wurden ohne meine Mitarbeit in der Arbeitsgruppe „Translationale Krebsforschungsgruppe“ der Klinik I für Innere Medizin der Universitätsklinik Köln durch Frau Dr. med. Mariia Cherviakova erstellt und mir zur Verfügung gestellt.

Die in dieser Arbeit angegebenen Experimente sind nach entsprechender Anleitung durch Frau Dr. med. Tamina Seeger-Nukpezah, Frau Dr. Nelly Mikhael und Herrn Prof. Dr. med. Jochen Fries von mir selbst ausgeführt worden.

Erklärung zur guten wissenschaftlichen Praxis:

Ich erkläre hiermit, dass ich die Ordnung zur Sicherung guter wissenschaftlicher Praxis und zum Umgang mit wissenschaftlichem Fehlverhalten (Amtliche Mitteilung der Universität zu Köln AM 132/2020) der Universität zu Köln gelesen habe und verpflichte mich hiermit, die dort genannten Vorgaben bei allen wissenschaftlichen Tätigkeiten zu beachten und umzusetzen.

Köln, den 03.09.2023

Unterschrift:

Danksagung

Als erstes möchte ich mich bei der Leiterin der translationalen Krebsforschungsgruppe der Klinik I für Innere Medizin der Uniklinik Köln, Frau Dr. med. Tamina Seeger-Nukpezah bedanken. Vielen Dank für die Möglichkeit meine Doktorarbeit in dieser Forschungsgruppe ablegen zu können und die Hilfe während des gesamten Projektes.

Als nächstes möchte ich mich herzlich bei Herrn Prof. Dr. med. Christian Pallasch für die offizielle Betreuung dieser Promotion bedanken.

Ein besonderer Dank geht an Frau Dr. Nelly Mikhael, die mir während des gesamten Prozesses, von den Experimenten bis zur Verfassung dieser Promotionsschrift, immer mit Rat und Tat zur Seite gestanden hat.

Vielen Dank an Herrn Prof. Dr. med. Jochen Fries für die Anleitung zur histologischen Auswertung.

Danke auch an alle Mitglieder der translationalen Krebsforschungsgruppe und die anderen Mitarbeiter im Haus 16 für die Unterstützung während meines Projektes.

Mein abschließender und ganz besonderer Dank geht an meine Mutter, die mich sowohl während des Studiums und während dieses Projektes immer unterstützt hat und mir auch auf meinem weiteren Lebensweg immer und jederzeit zur Seite steht.

Meiner Mutter

Inhaltsverzeichnis

Abbreviations

Abl	-	tyrosine-protein kinase ABL1
ADPKD	-	autosomal dominant polycystic kidney disease
AhR	-	aryl hydrocarbon receptor
AKT	-	protein kinase B
ATP	-	adenosine triphosphate
AURKA	-	aurora kinase A
Balb/c	-	Bagg's albino
BCAR1	-	breast cancer anti-estrogen resistance protein 1
BCR	-	breakpoint cluster region
Blk	-	B lymphocyte kinase
BrdU	-	bromodeoxyuridine
BSA	-	bovine serum albumin
CAS	-	Crk-associated substrate
CAS-L	-	Crk-associated substrate-related protein
ccRCC	-	clear-cell renal cell carcinoma
cDNA	-	complementary desoxyribonucleic acid
CML	-	chronic myelogenous leukemia
CRK	-	CRK proto-oncogene
cRNA	-	complementary ribonucleic acid
CTLA-4	-	cytotoxic T-lymphocyte-associated protein 4
CTTN	-	cortactin
DNA	-	desoxyribonucleic acid
DOCK1	-	dedicator of cytokinesis 1
DOCK3	-	dedicator of cytokinesis 3
dsDNA	-	double-stranded desoxyribonucleic acid
ECM	-	extracellular matrix
ECT2	-	epithelial cell transforming 2
EFS	-	embryonal Fyn-associated substrate
ErbB	-	erythroblastosis oncogene B
ERK	-	extracellular signal-regulated kinase
FACS	-	fluorescence-activated cell sorting
FAK	-	focal adhesion kinase
FBS	-	fetal bovine serum
FGF	-	fibroblast growth factor
Fgr	-	Gardner-Rasheed Feline Sarcoma Viral (V-Fgr) Oncogene Homolog

FLCN	-	folliculin
FOV	-	field of view
Fyn	-	proto-oncogene tyrosine-protein kinase Fyn
GFP	-	green fluorescent protein
GRB2	-	growth factor receptor-bound protein 2
HE	-	hematoxylin and eosin
Hck	-	hematopoietic cell kinase
HDAC6	-	histone deacetylase 6
HEF1	-	human enhancer of filamentation 1
HEPL	-	HEF1-EFS-p130Cas-like
HGFR	-	hepatocyte growth factor receptor
HIF	-	hypoxia-inducible factor
HTLV-1	-	human T-cell lymphotropic virus type 1
IL-2	-	interleukin 2
IMDC	-	International Metastatic RCC Database Consortium
IRS	-	insulin receptor substrate
IVT	-	*in vitro* transcription
JNK	-	c-Jun N-terminal kinase
Ki-67	-	marker of proliferation Ki-67
Kras	-	Kirsten rat sarcoma virus
Lck	-	leukocyte C-terminal Src kinase
Lyn	-	Lck/Yes-related novel protein tyrosine kinase
MEF	-	mouse embryonic fibroblast
MET	-	MET proto-oncogene
miRNA	-	micro ribonucleic acid
MMP	-	matrix metalloproteinase
mRCC	-	metastasized renal cell carcinoma
mTOR	-	mammalian target of rapamycin
NEDD9	-	neural precursor cell expressed developmentally down-regulated protein 9
NOD	-	non-obese diabetic
ns	-	not significant
NSCLC	-	non-small cell lung cancer
NSG	-	NOD SCID gamma
PAK1	-	p21 (RAC1) activated kinase 1
PAK2	-	p21 (RAC1) activated kinase 2
PCR	-	polymerase chain reaction

PD-1	-	programmed cell death protein 1
PDGFR	-	platelet-derived growth factor receptor
PD-L1	-	programmed death ligand 1
PI3K	-	phosphoinositide 3-kinases
Pkd-1	-	polycystic kidney disease 1
PTEN	-	Phosphatase and Tensin homolog
PTK	-	phosphotyrosine kinase
qPCR	-	real-time quantitative polymerase chain reaction
RAC	-	Ras-related C3 botulinum toxin substrate
RAS	-	rat sarcoma virus
RCC	-	renal cell carcinoma
RET	-	rearranged during transfection
RhoA	-	Ras homolog family member A
RNA	-	ribonucleic acid
RT	-	room temperature
RTK	-	receptor tyrosine kinase
SCID	-	severe combined immunodeficiency
SD	-	standard deviation
SH3	-	Src-homology 3
shRNA	-	short hairpin ribonucleic acid
- shNT	-	non targeted shRNA
- shA	-	shRNA NEDD9 A
- shB	-	shRNA NEDD9 B
- shC	-	shRNA NEDD9 C
- shD	-	shRNA NEDD9 D
SOS	-	Son of Sevenless
Src	-	proto-oncogene tyrosine-protein kinase Src
STK	-	serine/threonine kinase
TGF-ß	-	transforming growth factor beta
TP53	-	tumor protein p53
VEGF	-	vascular endothelial growth factor
VEGFR	-	vascular endothelial growth factor receptor
VHL	-	Von Hippel-Lindau
Yes	-	proto-oncogene tyrosine-protein kinase Yes
Yrk	-	Yes-related kinase
ZNF384	-	zinc finger protein 384

1. Zusammenfassung

Die Fallzahlen des Nierenzellkarzinoms sind im Verlauf der letzten Jahre stetig angestiegen. Bislang konnten die genaue Pathogenese sowie die verantwortlichen deregulierten Signalwege nicht entschlüsselt werden. Zusätzlich existieren keine Biomarker, die die Therapieauswahl leiten und ein Therapieansprechen vorhersagen können. NEDD9 ist ein Gerüstprotein, welches nach derzeitigem Wissensstand mit einer Vielzahl onkogener Kinasen in verschiedenen Krebsentitäten wie zum Beispiel dem pulmonalen Adenokarzinom, Brustkrebs und Leukämie interagiert. In den meisten Krebsentitäten nimmt NEDD9 die Rolle eines tumortreibenden Proteins ein und ist mit einer schlechten Prognose sowie schlechtem Therapieansprechen assoziiert. Bis dato gibt es nur wenige Daten bezüglich der Rolle von NEDD9 im Nierenzellkarzinom; lediglich eine Forschungsgruppe zeigte eine erhöhte Expression von NEDD9 in Gewebe des Nierenzellkarzinoms in Vergleich zu physiologischem Nierengewebe und eine andere Gruppe zeigte, dass NEDD9 das Verhalten von RCC-Zellen beeinflusst.

Das Ziel dieser Arbeit ist es die Rolle von NEDD9 im Nierenzellkarzinom aufzuklären. Die Ergebnisse zeigen, dass eine erhöhte NEDD9-Expression *in vivo* zu einem aggressiveren histologischen Phänotyp in syngenen und Xenograft-Maus-Modellen führt.

In einem Kinom-Assay zeigt sich, dass die Expression von NEDD9 mit der erhöhten Aktivität von Kinasen der Src-Familie in murinen RCC-Zellen und der Aktivierung von Kinasen, des VEGF/FGF-Weges in menschlichen RCC-Zellen einhergeht. Dieser Zusammenhang wurde durch eine Gen-Microarray-Analyse weiter beleuchtet. Hierbei veränderte die NEDD9-Defizienz die Expression verschiedener bekannter onkogener Kinasen und Signalwege. Insbesondere wurde eine signifikante Herabregulierung in wichtigen Signalwegen wie HIF, EGFR, VEGFR2, PDGFR und dem PI3K/AKT-Signalweg beobachtet.

Zusammenfassend deuten die Ergebnisse darauf hin, dass NEDD9 als molekularer Knotenpunkt die Pathogenese des Nierenzellkarzinoms fördert, indem es verschiedene onkogene Signalwege aktiviert. Weitere Untersuchungen sind erforderlich, um die genaue Interaktion von NEDD9 und diesen Signalwegen in der Pathogenese des Nierenzellkarzinoms zu beleuchten, um den Weg für neue gezielte Therapien bei dieser Erkrankung zu ebnen.

2. Summary

The number of new cases of renal cell carcinoma (RCC) have increased steadily over the last years. However, to date, the pathogenesis and underlying deregulated pathways in RCC remain to be deciphered. In addition, biomarkers that could dictate treatment regimens and predict response to different available treatments have yet to be discovered. NEDD9 is a scaffolding protein known to interact with a multitude of oncogenic kinases in different cancer entities such as lung adenocarcinoma, breast cancer as well as leukemias among others. In most cancer entities, NEDD9 acts as a tumor driver and has been associated with poor prognosis and response to treatment. Data on the role of NEDD9 in RCC is scarce with only one research group demonstrating increased NEDD9 expression levels in RCC tissue compared to normal renal tissue and another group showing NEDD9 influencing RCC cell behavior.

The aim of this work was to further elucidate the role of NEDD9 in RCC. The results show that NEDD9 leads to a more aggressive histologic phenotype *in vivo* in syngeneic and xenograft mouse models. In a kinome assay, NEDD9 expression is linked to the increased activity of Src family kinases in murine RCC cells and the activation of kinases belonging to the VEGF/FGF pathway in human RCC cells. This relationship has been further illuminated through gene microarray analysis. Notably, the deficiency of NEDD9 has demonstrated a substantial impact on various known oncogenic kinases and pathways. In particular, significant downregulation was observed in crucial pathways such as HIF, EGFR, VEGFR2, PDGFR and the PI3K/AKT pathway.

Taken together, these findings suggest that NEDD9 acts as a molecular hub influencing the development of RCC by engaging with a spectrum of well-established oncogenic pathways. Further studies are needed to elucidate the precise interplay of NEDD9 and these signaling pathways in the pathogenesis of renal cell carcinoma, paving the way for new targeted therapies in this disease.

3. Introduction

3.1 Renal cell carcinoma

3.1.1. Epidemiology

In the year 2020, renal cell carcinoma (RCC) (including the renal pelvis) was in place 14 in the number of new cancer cases with 431,288 new cases worldwide. In Europe, RCC (including the renal pelvis) ranked at number 9 with 138,611 new cases in 2020[1].

Demographic as well as socioeconomic factors appear to play an incomprehensible role in the development of RCC with patients from developed countries accounting for approximately 59% of all cases[2,3]. The difference in incidence between the sexes is striking. Men seem to suffer more often from RCC; in the year 2020 63% of all RCC cases worldwide were men[1]. The role of the patients' sex has not been clarified to date.

The International Agency for Research on Cancer (IARC) predicts that RCC cases are going to increase by up to 57.8% until the year 2040 when compared to worldwide cases in 2020[4].

RCC is often detected during routine ultrasound or other abdominal imaging procedures. Patients develop rather late vague symptoms such as flank pain, palpable retroperitoneal mass and hematuria[3,5,6]. Therefore, patients are usually diagnosed in later stages of RCC and thus have a poor prognosis. When metastasized, 5-year relative survival of RCC patients is around 15%; in the localized stage the survival is over 90%[7].

3.1.2. Etiology and risk factors

96% of clear-cell RCC (ccRCC) cases are associated with biallelic mutation or loss of the von Hippel-Lindau (VHL) tumor suppressor gene leading to its inactivation[8,9]. In about 4% of cases, the defective gene is inherited and causes the autosomal dominant von Hippel-Lindau cancer syndrome, which leads to a higher risk of several cancers such as ccRCC, pheochromocytoma and hemangioblastoma[10–12]. Inactivation of VHL leads to an increase of hypoxia inducible factors (HIFs), which act as transcriptional factors and activate genes responsible for a cells' response to hypoxia, including cell migration, metabolism, and angiogenesis[9,13].

Other known hereditary syndromes that are accompanied with RCC include the following: for papillary RCCs the hereditary papillary RCC and the hereditary syndrome of leiomyomatosis and RCC, for ccRCCs the tuberous sclerosis complex and for chromophobe RCCs the Birt-Hogg-Dube Syndrome[7,13,14]. However, only circa 4% of all RCC cases are caused by a hereditary syndrome and the rest presumably through different acquired sporadic mutations[12,14]. In mice, VHL inactivation alone was not able to cause ccRCC[15], so it seems that additional mutations have to occur in order to develop ccRCC. Further mutations that appear

to be common in ccRCC include the loss of chromosome 3p and genes involved in chromatin remodeling, histone modifiers and the mTOR pathway[12,13,16].

For papillary RCC, the most prevalent mutations lie in the proto-oncogene MET, EGFR (epidermal growth factor receptor), and the gene for fumarate hydratase, whereas in chromophobe RCC most mutations are seen in tumor suppressor genes PTEN (phosphatase and tensin homolog), the folliculin gene FLCN and TP53 (tumor protein p53)[6,17].

Further known risk factors for RCC include lack of physical activity, obesity, exposure to trichloroethylene, alcohol consumption, arterial hypertension and cigarette smoking[2,6,18,19].

3.1.3. Classification

Traditionally, RCCs are divided into different subgroups based on their histological appearance. The most common entity is clear-cell RCC with around 70%, followed by papillary (10-15%), chromophobe (4-6%), collecting duct (<1%) and other unclassified (4-5%) RCCs[14,20].

In addition to the histological classification, the macroscopic extent of the tumor is classified using the worldwide approved and commonly used TNM-classification. This classification is based on three different categories: the dimension of the primary tumor (T), the involvement of lymph nodes (N) and the spread of metastases (M). Table 1 shows the classification for renal tumors[21].

Primary Tumor (T):	
TX	Primary tumor cannot be assessed
T0	No evidence of primary tumor
T1	Tumor ≤ 7cm in greatest dimension, limited to kidney
T1a	Tumor ≤ 4cm in greatest dimension, limited to kidney
T1b	Tumor > 4cm but ≤ 7cm in greatest dimension, limited to kidney
T2	Tumor > 7cm in greatest dimension, limited to kidney
T2a	Tumor > 7cm but ≤ 10cm in greatest dimension, limited to kidney
T2b	Tumor > 10cm, limited to kidney
T3	Tumor extends into major veins or perinephric tissues but not into the ipsilateral adrenal gland and not beyond Gerota's fascia
T3a	Tumor grossly extends into the renal vein or its segmental (muscle containing) branches, or tumor invades perirenal and/or renal sinus fat but not beyond Gerota's fascia
T3b	Tumor grossly extends into the vena cava below the diaphragm
T3c	Tumor grossly extends into the vena cava above the diaphragm or invades the wall of the vena cava

T4	Tumor invades beyond Gerota's fascia (including contiguous extension into the ipsilateral adrenal gland)
Lymph nodes (N):	
NX	Regional lymph nodes cannot be assessed
N0	No regional lymph node metastasis
N1	Metastasis in regional lymph node(s)
Distant metastasis (M):	
M0	No distant metastasis
M1	Distant metastasis

Table 1: TNM-Classification for renal tumors. Adapted from Brierley, Gospodarowicz, and Wittekind 2017[21].

The most common metastatic sites in ascending order are brain, adrenal gland, liver, lymph nodes, bone and lung[22]. Through the different ranks in the three main categories, patients can be assigned to four stages (Table 2). Stage I tumors are relatively small and locally limited to the kidney. In the following stage, the tumor is still limited to the kidney, but has an increased mass. Tumors from stage III have either advanced into tissue surrounding the kidney or have spread to regional lymph nodes. In stage IV metastases in distant organs or a local progress beyond the Gerota's fascia are detected. These different stages correlate with prognosis. In stage I 5-year survival is at 89.6%, in stage II at 82.7%, followed by 57.7% in stage III and 18.3% in the advanced stage IV[23].

Stage	**TNM-Status**
Stage I	T1, N0, M0
Stage II	T2, N0, M0
Stage III	T1 or T2, N1, M0 T3, N0 or N1, M0
Stage IV	T4, any N, M0 Any T, any N, M1

Table 2: Anatomic stages and prognosis groups of renal cell carcinoma. Adapted from Amin et al. 2017[24].

3.2 Therapy

As ccRCC is the most common RCC subtype, most clinical trials have been conducted with ccRCC; thus, the following therapy algorithms apply to the treatment of ccRCC.

When no distant metastasis is evident and the tumor is limited to the kidney, partial or radical nephrectomy is the preferred treatment option[13,19,25].

Treatment of metastasized ccRCC is difficult to date, as RCC is mostly resistant to conventional radio- and chemotherapy. Additionally, some patients with metastasized ccRCC appear to be non-responders to any available treatment[26–28]. Despite the improvement of already existing and the discovery of multiple new agents during the last years, eventually nearly all patients acquire tumor resistance and experience disease progression[9,27,29–31]. Nevertheless, outcomes of patients have improved through the newly discovered therapy options. Before the growing use of targeted therapies, two-year survival of patients with metastatic ccRCC was less than 20%[29]. During this time, cytokines like high dose interleukin 2 (IL-2) or interferon alpha were important pillars in systemic treatment, but were not able to show superiority over targeted therapies[13,32].

Today, systemic therapy for metastasized ccRCC consists of combinations of agents from the following three groups:

1. Multi-tyrosine-kinase inhibitors (TKI) targeting different kinases like VEGF (vascular endothelial growth factor) or PDGF (platelet-derived growth factor) receptors, c-KIT, and MET like sunitinib, pazopanib, cabozantinib, lenvatinib, and axitinib as well as the VEGF antibody bevacizumab. RCCs and particularly ccRCCs are known to be highly vascularized tumors[9,14,31,33] and the VEGF pathway has been shown to play an important role in the development of RCC[9].

2. Immune checkpoint inhibitors (ICI) including PD-1 (programmed cell death protein 1; agents nivolumab and pembrolizumab), PD-L1 (programmed cell death ligand 1) checkpoint inhibitors (avelumab and atezolizumab) and anti-CTLA-4 (cytotoxic T-lymphocyte associated protein 4) antibodies (ipilimumab). One of the hallmarks of cancer is its ability to escape the detection and subsequent destruction by our immune system[34]. PD-1 and CTLA-4 are expressed on T cells and both have an inhibitory effect on T cell response. Different cancer cells were shown to express the ligand to PD-1, namely PD-L1, and thereby downregulating antitumor processes of T cells. The co-stimulatory molecules to CTLA-4, CD80/85, are expressed by antigen presenting cells and are normally important in regulating the immune response, so that the response is neither too intense nor too long. In the face of a tumor, it is beneficial to have a more intense T cell response to eliminate tumor cells. This can be achieved by blocking either the inhibitory proteins PD-1 and CTLA-4 directly or by blocking the ligand PD-L1[35]. In RCC, immune checkpoint inhibitors as monotherapy or combination therapy have been shown to have significantly increased rate of progression free survival and overall survival when compared to monotherapy with sunitinib[36–39].

3. mTOR (mammalian target of rapamycin) inhibitors like temsirolimus and everolimus.

In RCC, several different mutations upstream as well as downstream of mTOR have been found. Through the more sufficient and convincing data regarding VEGF or other multi-kinase inhibitors as well as immune checkpoint inhibitors, the role of mTOR inhibitors at the moment

is more as a second-line after patient progressed or had adverse effects under therapy with ICIs or TKIs[19,40].

To decide which therapy regimen is best for the specific patient based on their prognosis, the IMDC score (International mRCC Database Consortium Prognostic Model), also known as Heng criteria, is most commonly used[40]. This score consists of the following six risk factors:

1. hemoglobin concentration less than the lower limit of reference value
2. time from initial diagnosis to treatment less than a year
3. Karnofsky status performance less than 80%
4. platelet count higher than the upper limit of reference value
5. neutrophil count higher than the upper limit of reference value
6. corrected calcium concentration higher than 10mg/dL.

Through these criteria, patients are separated into three different risk groups: the favorable (no risk factors), intermediate (1-2 risk factors) and the poor risk group (≥3 risk factors)[41].

According to current German and European guidelines as well as current clinical trials, first-line therapy for mRCC is as follows:

For all risk profiles the standard consists of a combination of an immune checkpoint inhibitor and a multi-tyrosine kinase inhibitor (for example, nivolumab plus cabozantinib). If there are contraindications to the combination therapy, the treatment options are bevacizumab plus interferon alpha or pazopanib, sunitinib or tivozanib as a monotherapy.

In the intermediate and poor risk profile, a combination of the two immune checkpoint inhibitors nivolumab and ipilimumab represents the first line treatment. If combination therapy is not possible, capozantinib or sunitinib as monotherapy are other options.

The second-line treatment is identical in all risk profiles and consists of lenvatinib plus everolimus or nivolumab or capozantinib as a monotherapy. Other options include monotherapy of axitinib, sunitinib, everolimus, pazopanib, and sorafenib[31,36–39,42,43].

Although a lot of progress has been made in the treatment of RCC, a significant number of patients experience primary treatment failure[40,44,45]. After confirmation of tumor progress under the first-line treatment, it is advised to switch to a different agent group[40,42] to bypass possible developed escape mechanisms or to treat a resistant tumor cell clone, that was selected under the prior treatment[6,46].

3.3 Scaffolding protein NEDD9

3.3.1. Scaffolding proteins

In 2009, Shaw and Filbert described four main functions for scaffolding proteins: 1. To cluster different components of a signaling pathway in close proximity to each other 2. Localize this signaling pathway to a specific part of the cell 3. Increase or decrease the activity of the signaling pathway via influencing positive and negative feedback mechanisms 4. To protect

activated proteins from deactivation or degradation[47]. In summary, scaffolding proteins serve as molecular hubs to coordinate and enhance protein-protein interactions within the cell in space and time[48,49]. By targeting scaffolding proteins instead of deregulated kinases there are several possible advantages. By blocking a scaffolding protein, it is possible to target multiple different pathways or several proteins of one pathway that converge on one scaffolding protein. Further, only deregulated pathways could be targeted and side effects could be reduced by sparing normally functioning pathways. By targeting scaffolding proteins, the inhibition of deregulated kinases is different than direct kinase inhibition via a targeted therapy, thus creating a possibility to bypass acquired resistance to targeted agents.

3.3.2. CAS protein NEDD9

Crk-associated substrate (CAS) proteins are non-catalytic scaffolding proteins. To this date there are four members of this protein group: BCAR1 (breast cancer resistance 1), EFS (embryonal Fyn substrate), HEPL (HEF1-EFS-p130Cas-like) and NEDD9 (neural precursor cell expressed, developmentally downregulated 9)[50]. NEDD9 is also known as CAS-related protein, lymphocyte type (CAS-L) and human enhancer of filamentation 1 (HEF1) and is localized on chromosome 6p25-p24 in the human genome.

Specific for CAS proteins is their carboxy terminal containing a highly preserved motif. It has been predicted, that this terminal includes a helix-loop-helix domain[51], which is able to fit to the focal adhesion targeting domain (FAT) of focal adhesion kinase (FAK), so that it is now described as FAT-homologous region[52]. At the beginning of cell adhesion, this terminal gets phosphorylated and is therefore creating new binding sites. At its amino-terminal NEDD9 harbors a SH3 (Src homology 3) domain, that is able to bind to polyproline motifs of other proteins like the most studied interaction partner FAK[50,53]. These interactions allow CAS proteins including NEDD9 to significantly impact the regulation in different cell mechanisms such as cell spreading, migration, invasion and formation of adhesions[54]. Between these two terminals is an unstructured substrate domain and a four-helix bundle forming consisting of a serine rich region[55] (Fig. 1).

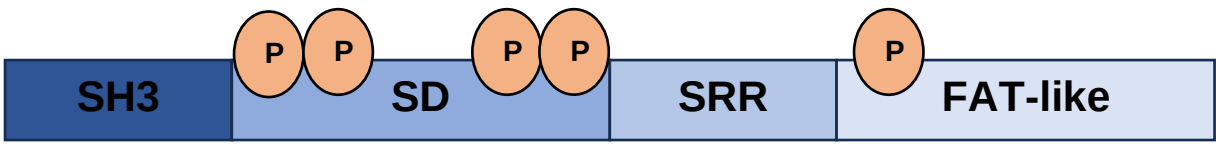

Figure 1: Schematic structure of NEDD9. SH3 = Src homology 3 domain, SD = substrate domain, SRR = serine rich region, FAT-like = focal adhesion targeting domain. Adapted from Shagisultanova et al[55]

NEDD9 expression levels are variable between different cell types and different cell environments[50]. NEDD9 transcription is increased by TGF-ß, all-trans retinoic acid, progesterone receptor A, hypoxia and dioxin (through AhR), but its expression is mostly regulated on protein level. Serum-containing growth factors cause NEDD9 to accumulate and to be hyperphosphorylated and cells to enter cell cycle. Additionally, NEDD9 is regulated by miR-145 and miR-125b[50,55,56]. In VHL deficient cells, NEDD9 expression is increased by high levels of the transcription factor HIF-2α[57].

With a molecular weight of 93kDa, NEDD9 can be detected as a double band at 105 and 115kDa in protein analyses. This discrepancy is due to extended phosphorylation that CAS proteins are known to undergo[58]. When attached, the expression of its 115kDa form is increased in comparison to suspension cells, where 105kDa NEDD9 is predominant[59]. In addition, phosphorylation of NEDD9 is influenced by the process of the cell cycle, hypoxia and interaction partners that directly phosphorylate NEDD9 like PDGFR (platelet-derived growth factor receptor) and G-protein coupled receptors[50].

3.3.3. Function of NEDD9 and interactions

NEDD9 is known to play a role in focal adhesions as well as the mitotic spindle, centrosomes and the base of the primary cilium[50,58]. In interaction with FAK, NEDD9 localizes at focal adhesions and increases their stability and therefore slowing down cell migration. After binding to NEDD9, FAK phosphorylates the C-terminal creating a binding site for Src-family kinases. After binding they create further binding motifs for proteins that directly support the process of cell spreading[50,53,60]. In T cells, NEDD9 is involved in integrin signaling, that promotes cell migration[59].

Another function of NEDD9 is in the course of mitosis. An important interaction partner during mitosis is the kinase Aurora A (AURKA). AURKA regulates the correct separation of chromosomes. Important for this process is the timed activation and inactivation of AURKA. NEDD9 has been shown to play a role in activating AURKA. But when AURKA is overexpressed or too active, chromosomes do not separate correctly[50]. Following induced NEDD9 expression, mitotic cells failed in 37-56% to complete mitosis. In contrast to that, depletion of NEDD9 causes asymmetric spindle formation leading cells to not enter or complete mitosis, generating multinucleated cells. To cycle through mitosis correctly, timely increase and decrease of NEDD9 or interaction with its different interaction partners plays an important role[59,61] (see Fig. 2).

3.3.4. NEDD9 in cancer and other diseases

Known oncogenic proteins such as Crk, BCR (breakpoint cluster region)-Abl, FAK, PI3K (Phosphoinositide 3-kinase)/AKT and Src are known to be interaction partners of NEDD9, suggesting a role of NEDD9 in several cancer entities (see Fig. 2).

It has been shown that NEDD9 positively influences early tumor formation in breast cancer and promotes metastases and migration in glioblastoma. Further, hyperphosphorylated NEDD9 was found in hematological malignancies such as HTLV-1(human T-lymphotrophic virus type 1)-associated T-cell, acute lymphoplastic and chronic myelogenous leukemia. High NEDD9 expression levels were correlated with higher numbers of metastases in melanoma and renal cell carcinoma[50,54,55,62–64]. In prostate cancer and in non-small cell lung cancer NEDD9 seems to be overexpressed in comparison to healthy tissue[54]. In ovarian cancer high NEDD9 expression levels are associated with a more aggressive disease and a mesenchymal/stem-cell like phenotype[65]. Gu et al. showed that elevated NEDD9 expression levels are connected to poor prognosis in several solid cancers such as lung cancer, gastric cancer, bladder carcinoma, breast cancer, colorectal cancer, pancreatic carcinoma and hepatocellular carcinoma[66,67]. However, the overexpression of NEDD9 alone does not appear to be able to induce tumorigenesis, but is only supporting tumorigenesis in the context of other existing oncogenes[55]. Contrary to these findings, deletion of NEDD9 in a transgenic mouse model imitating BCR-Abl-associated leukemia led to a more aggressive disease[54] as well as in a model of non-small cell lung cancer (NSCLC) driven by Kras (Kirsten Rat Sarcoma virus) mutation and Tp53 loss, where depletion of NEDD9 led to an increased tumor mass[68].

Taken together, the impact of NEDD9 as a tumor suppressor or tumor driver is context-dependent and seems to depend on the type of tumor and its deregulated signaling pathways. Furthermore, there are findings associating NEDD9 with other diseases besides cancer. A specific single-nucleotide polymorphism of NEDD9 is assumed to increase vulnerability for a late-onset form of Alzheimer's disease[69]. In a mouse model mimicking autosomal dominant polycystic kidney disease (ADPKD), loss of NEDD9 increased the number of cysts in Pkd1-deficient mice. This was correlated to the finding that cysts composed of NEDD9-deficient renal cells have deformed cilia[70]. After transient cerebral ischemia NEDD9 is increased in the cerebral cortex and hippocampus and induces outgrowth of neurons[55].

3.3.5. NEDD9 in RCC

To date, the data on the role of NEDD9 in RCC are sparse. In 2014 Wang et al. showed that NEDD9 levels are higher in RCC tissue and RCC 786-O and Caki 1 cell lines compared to normal renal tissue. NEDD9 knockdown in these cell lines seemed to enhance apoptosis and inhibit cell cycle[71]. In a collective of 68 patients with RCC, elevated NEDD9 levels were significantly associated with shorter overall survival. Following knockdown of NEDD9, RCC

cell lines showed decreased migration and invasion[63]. In RCC cells with VHL deficiency - the most common genetic aberrance in ccRCC - NEDD9 levels were elevated. Low levels of NEDD9 in VHL-deficient cells are associated with correct cilia formation, which is in contrast with a model of autosomal-dominant polycystic kidney disease, where low levels of NEDD9 in Pkd1-deficient cells was associated with incorrect cilia formation[57,70].

To this date, treatment of RCC, especially when metastasized, is complicated due to the fact that the pathophysiology is not completely elucidated as well as the lack of reliable biomarkers to predict treatment response. In the past years it has been shown, that NEDD9 plays an important role in deregulated pathways of different cancer entities and that the prognosis of these cancers often correlates with high NEDD9 levels. In RCC, NEDD9 overexpression has been observed to predict poor prognosis. Xu et al. were able to show that in ccRCC cells, NEDD9 mRNA levels were increased upon VHL loss. Furthermore, they were able to demonstrate that NEDD9 is regulated by HIF-2α, a downstream effector of VHL. After loss of VHL, which is the most common genetic aberrance observed in ccRCC, HIFα and its subunits accumulate and lead to the transcription of multiple different genes, mostly involved in cell migration, metabolism, and angiogenesis[9,13,57]. Looking at this known interaction between VHL or more precisely its downstream effectors and NEDD9 makes NEDD9 an interesting target for further research in ccRCC. It appears to be a good starting point to elucidate the deregulated pathways underlying the pathogenesis of ccRCC as NEDD9 itself or its downstream interaction partners could be used to 1. detect novel treatment targets 2. be used as prognostic markers for the progress of RCC 3. be used as biomarkers to predict treatment response to specific agents.

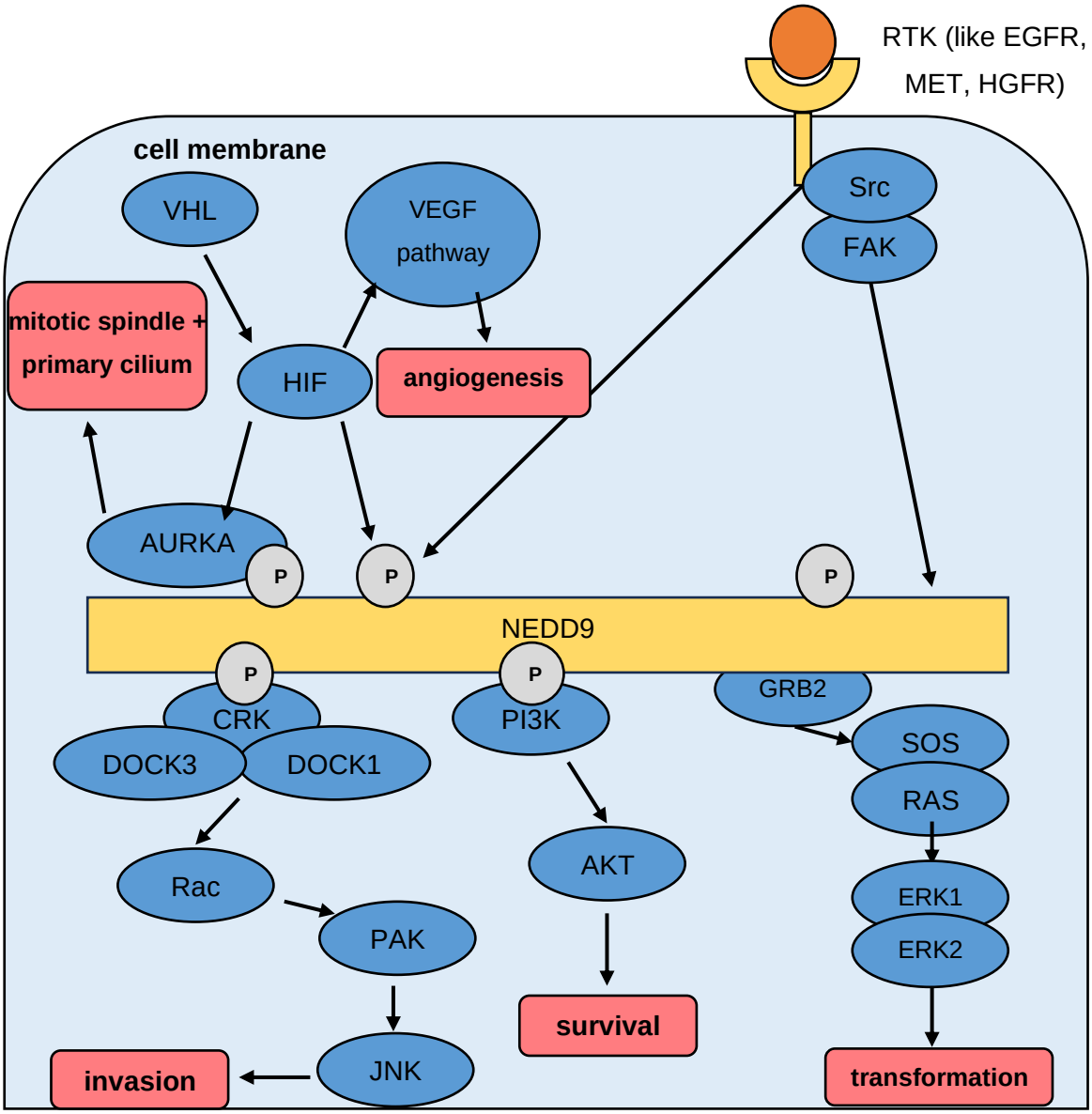

Figure 2: Schematic structure of NEDD9 with its known interaction partners and effects. Adapted and amended from Cabodi et al[96] and Shagisultonova et al[55]

3.4 Aims

To further determine the role of NEDD9 in RCC, this thesis addressed three main aims.

The first aim was to validate whether NEDD9 alterations and its subsequent effects are conserved in other ccRCC cell lines, namely the human RCC cell line A498, which expresses low endogenous levels of NEDD9. The initial aim was to generate A498 cells that are stably overexpressing NEDD9 and consequently perform functional tumor assays to compare NEDD9-overexpressing and -wild A498 cells regarding cellular processes known to be influenced by NEDD9 in other tumor entities as well as RCC including cellular proliferation, viability, invasion and apoptosis.

The second aim was to evaluate the effect of NEDD9 in ccRCC *ex vivo*. Histologic H&E-stained slides of a xenograft and a syngeneic model from primary tumors as well as metastatic organs[72] were analyzed for tumor incidence, tumor size/number of tumor nodules, number of mitotic cells and giant cells. Additionally, tumor slides of both mouse models were stained for the proliferation marker Ki67 and the apoptosis marker Caspase 3.

The third aim was to identify the underlying signaling pathways and their effect on the cellular processes of ccRCC *in vitro*. For this aim, gene arrays were performed comparing NEDD9-competent to NEDD9-deficient human 786-O ccRCC cells. Additionally, to elucidate potential interaction partners of NEDD9, phosphotyrosine kinase (PTK) and serin/threonine kinase (STK) array chips were used to determine the differential global kinomic activity in primary tumors derived from NEDD9-competent or -deficient cells.

4. Materials and Methods

4.1 Materials

4.1.1. Chemicals and reagents

Chemical/reagent	Art./Cat. No.	manufacturer
2-Mercaptoethanol	4227.1	AppliChem GmbH Darmstadt, Germany
Agar Bacteriology grade	A0949.0250	AppliChem GmbH Darmstadt, Germany
Ammonium persulfate	9592.3	Carl Roth GmbH Karlsruhe, Germany
Ampicillin Sodium Salt BioChemica	A0839	AppliChem GmbH Darmstadt, Germany
Ampuwa sterile water	1080181	Fresenius Kabi Deutschland GmbH Bad Homburg, Germany
Bromophenol blue	A2331	AppliChem GmbH Darmstadt, Germany
cOmplete Protease Inhibitor Cocktail	04693116001	F. Hoffmann-La Roche AG Basel, Switzerland
DMSO (*Dimethyl sulfoxide*)	20385	Serva Electrophoresis GmbH Heidelberg, Germany
DPBS (*Dulbecco's Phosphate-Buffered Saline*)	14190094	Life Technologies GmbH Darmstadt, Germany
EGTA (*ethylene glycol-bis (β-aminoethyl ether)-N, N, N', N'-tetra acetic acid*)	A0878	Applichem GmbH Darmstadt, Germany
Ethanol absolute for molecular biology	A3678	AppliChem GmbH Darmstadt, Germany
FBS (*Fetal Bovine Serum*) Superior	S0615	Biochrom GmbH Berlin, Germany
GeneJuice® Transfection Reagent	70967	Merck KGaA Darmstadt, Germany
Glycerol	3783.1	Carl Roth GmbH Karlsruhe, Germany

Glycine	3790.2	Carl Roth GmbH Karlsruhe, Germany
HEPES (*4-(2-hydroxyethyl)-1-piperazineethanesulfonic acid*)	HN77.2	Carl Roth GmbH Karlsruhe, Germany
Isopropyl alcohol	6752.4	Carl Roth GmbH Karlsruhe, Germany
LB-Agar - Powder according to Miller	A0927	AppliChem GmbH Darmstadt, Germany
LB-Medium - Powder according to Miller	A0954	AppliChem GmbH Darmstadt, Germany
Lipofectamine 2000 Transfection Reagent	11668027	invitrogen Carlsbad, United States of America
Magnesium chloride	KK36.1	Carl Roth GmbH Karlsruhe, Germany
MEM *(Minimum Essential Medium)*	11095080	Life Technologies GmbH Darmstadt, Germany
MEM (*Minimum Essential Medium*) Non-Essential Amino Acids Solution (100X)	11140050	Life Technologies GmbH Darmstadt, Germany
Methanol	A3493	AppliChem GmbH Darmstadt, Germany
M-PER™ Mammalian Protein Extraction Reagent	78501	Thermo Fisher Scientific Rockford, United States of America
PhosSTOP	4906845001	F. Hoffmann-La Roche AG Basel, Switzerland
Pierce™ ECL Western Blotting Substrate	32106	Thermo Fisher Scientific Rockford, United States of America
Powdered milk, low fat	T145.2	Carl Roth GmbH Karlsruhe, Germany
Precision Plus™ Protein WesternC™ Standards	161-0376	BioRad Laboratories, Inc. Munich, Germany
Rotiphorese® Gel 30 (37,5:1)	3029.2	Carl Roth GmbH Karlsruhe, Germany

RPMI (*Roswell Park Memorial Institute*)1640 (1X) + GlutaMAX -I	61870	Life Technologies GmbH Darmstadt, Germany
SDS (*Sodium Dodecyl Sulfate*) grained pure	A7249	AppliChem GmbH Darmstadt, Germany
Sodium chloride	9265.2	Carl Roth GmbH Karlsruhe, Germany
Sodium fluoride	A3904	AppliChem GmbH Darmstadt, Germany
Sodium orthovanadate	A2196	AppliChem GmbH Darmstadt, Germany
Sodium pyrophosphate	1.06591.0500	VWR International GmbH Radnor, USA
SuperSignal™ West Femto Maximum Sensitivity Substrate	34094	Thermo Fisher Scientific Rockford, United States of America
TEMED (*Tetramethyl ethylenediamine*)	A1148	AppliChem GmbH Darmstadt, Germany
TRIS (*tris(hydroxymethyl)aminomethane*)	AE15.2	Carl Roth GmbH Karlsruhe, Germany
Triton® X100	3051.3	Carl Roth GmbH Karlsruhe, Germany
Trypsin-EDTA (0.5%), no phenol red	15400054	Life Technologies GmbH Darmstadt, Germany
Tryptone - Pancreatic digest of casein	T9410	Sigma Aldrich Munich, Germany
Tween® 20	9127.1	Carl Roth GmbH Karlsruhe, Germany
Yeast extract BioChemica	A1552	AppliChem GmbH Darmstadt, Germany

Table 3: Chemicals and reagents

4.1.2. Antibodies

Antibody (Ab)	Art./Cat. No.	manufacturer
Anti-mouse IgG, HRP-linked Ab (1:2500)	7076	Cell Signaling Technologies Inc. Danvers, United States of America

Anti-rabbit IgG, HRP-linked Ab (1:2500)	7074	Cell Signaling Technologies Inc. Danvers, United States of America
beta-Actin-mouse-HRP-linked-mAb (1:2500)	ab49900	Abcam Cambridge, United Kingdom
NEDD9-mouse-mAb (1:1000)	4044	Cell Signaling Technologies Inc. Danvers, United States of America

Table 4: Antibodies

4.1.3. Kits and arrays

Kit/Array	Art./Cat. No.	manufacturer
GeneChip™ 3' IVT PLUS Reagent Kit	902416	Thermo Fisher Scientific Rockford, United States of America
GeneChip™ Eukaryotic Poly-A RNA Control Kit	900433	Thermo Fisher Scientific Rockford, United States of America
GeneChip™ Human Genome U133 Plus 2.0 Array	900466	Thermo Fisher Scientific Rockford, United States of America
GeneChip™ Hybridization Control Kit	900454	Thermo Fisher Scientific Rockford, United States of America
GeneChip™ Hybridization, Wash, and Stain Kit	900720	Thermo Fisher Scientific Rockford, United States of America
JetStar™ 2.0 Plasmid Maxiprep Kit	220010	Genprice Inc. San Jose, United States of America
miRNeasy® Mini Kit	217004	Qiagen Hilden, Germany
Pierce™ BCA Protein Assay Kit	23225	Thermo Fisher Scientific Rockford, United States of America
Pierce™ Coomassie Plus (Bradford) Assay Kit	23236	Thermo Fisher Scientific Rockford, United States of America

Table 5: Kits and arrays

4.1.4. Buffers

Buffers	Components
0.5M Tris-HCl (pH 6.8)	250mM Tris
1.5M Tris-HCl (pH 8.8)	750mM Tris

6x Laemmli Buffer	0.35M Tris-HCl, 0.35mM SDS, 30% glycerol, 0.175mM bromophenol blue, 5% 2-mercaptoethanol
10x Running Buffer	250mM Tris, 1.92M glycine, 35mM SDS
10x TBS (pH 7.6)	0.2M Tris, 1.5M NaCl
10x Transfer buffer	250mM Tris, 1.5M NaCl
Lysis buffer (pH 7.5)	1% Triton, 50mM HEPES, 150mM NaCl, 1.5mM $MgCl_2$, 1mM EGTA, 100mM NaF, 10mM Na-pyrophosphate, 1mM Na_3VO_4, 10% glycerol
TBST	20mM 10x TBS, 0.1% Tween
Transfer Buffer	25mM 10x Transfer buffer, 20% methanol

Table 6: Buffers

4.1.5. Devices

Device	Art./Cat.No.	manufacturer
Branson Sonifier® 150D Ultrasonic Cell Disruptor	150D	Branson Ultrasonics Danbury, United States of America
ChemiDoc™ MP Imaging System	17001402	BioRad Laboratories, Inc. Munich, Germany
Countess™ II Automated Cell Counter	AMQAX1000	invitrogen Carlsbad, United States of America
- Countess™ Cell Counting Chamber Slides	C10228	
- Trypan blue stain (0.4%)	T10282	
GeneChip™ Hybridization Oven 645	00-0331	Thermo Fisher Scientific Rockford, United States of America
GeneChip™ Fluidics Station 450	00-0079	Thermo Fisher Scientific Rockford, United States of America
GeneChip™ Scanner 3000 7G System	00-0213	Thermo Fisher Scientific Rockford, United States of America

Heraeus HERAcell® 240i Incubator	390-4308	VWR International GmbH Radnor, United States of America
Heraeus Megafuge® 1.0	75003490	Heraeus GmbH Hanau, Germany
Invitrogen™ Magnetic Stand-96	AM10027	Thermo Fisher Scientific Rockford, United States of America
IX51 Inverted Microscope	IX51	Olympus Shinjuku, Japan
Mini-PROTEAN® Tetra Cell Systems	1658004	BioRad Laboratories, Inc. Munich, Germany
Thermo NanoDrop™ ND-1000 Spectrophotometer		Thermo Fisher Scientific Rockford, United States of America
Nucleofector™ II - Basic Nucleofector™ Kit for Primary Mammalian Epithelial Cells	VPI-1005	Lonza Group Ltd Basel, Switzerland
PamStation12®		PamGene International B.V. ‘s-Hertogenbosch, Netherlands
PowerPac™ Basic Power Supply	1645050	BioRad Laboratories, Inc. Munich, Germany
Sigma 1-14K	10020	Sigma Laborzentrifugen Osterode am Harz, Germany
SLG® Digital Dry Bath	BSH1002.E	Süd-Laborbedarf Gauting, Germany
Spectra Max M4 Microplate Reader	M4	Beckman Coulter GmbH Krefeld, Germany
Trans-Blot® Turbo™ Transfer System	1704150	BioRad Laboratories, Inc. Munich, Germany

Table 7: Devices

4.1.6. Software

Software	manufacturer
Adobe Illustrator	Adobe Inc. San Jose, United States of America
BioNavigator 6	PamGene International B.V. 's-Hertogenbosch, Netherlands
GraphPad Prism 10	GraphPad Software Inc. La Jolla, United States of America
ImageJ	National Institute of Health, United States of America
LabImage 1D	Kapelan Bio-Imaging Leipzig, Germany
Microsoft Office	Microsoft Redmond, United States of America
Olympus cell Sens Dimensions	Olympus Shinjuku, Japan
Partek® Genomics Suite® version 6.6	Partek Inc. Chesterfield, United States of America
SoftMax Pro 6.3	Molecular Devices Orleans Drive, United States of America

Table 8: Software

4.2 Methods

4.2.1. Cell culture

The human renal carcinoma cell lines 786-O and A498 and the murine Renca cell line were a kind gift by Prof. Dr. Bernhard Schermer (Department II of Internal Medicine, Cologne University Hospital). 786-O and Renca cells were cultured in RPMI-1640 medium, supplemented with 10% FBS; for the Renca cell line 1% sodium pyruvate, 1% non-essential amino acids and 1% L-glutamine were additionally supplemented. A498 cells were cultured in MEM medium, supplemented with 10% FBS. Cells were grown in a Heraeus incubator at 37°C, 5% CO_2 and passaged at 80% confluency by trypsinization at a dilution of 1:4 – 1:8.

4.2.2. NEDD9 depletion via shRNA

NEDD9 was depleted by lentiviral transfection of short hairpin RNA (shRNA) targeting murine (shN9-A and shN9-B) or human (shN9-C and shN9-D) NEDD9. Non-targeted (shNT) shRNA was used as control for murine and human cell lines.

DNA plasmids were obtained from the Golemis Lab at the Fox Chase Cancer Center, Philadelphia (USA). For lentivirus production, the generated plasmids were transfected into HEK293T cells using Lipofectamine 2000 according the manufacturer's instructions. HEK293t cells were co-transfected with helper plasmids and NEDD9 targeting constructs according to Carlotti et al[73]. Virus titer was quantified using HIV 1 p24 antigen enzyme-linked immunosorbent assay (ELISA) kit (ZeptoMetrix Corp.). The viral load was examined with a Multiplicity of Infection (MOI) of 1 for transduction. Polybrenes were used at a concentration of 8 µg/µl for a better transduction. Selection of transfected cells was induced by the cultivation of cells with puromycin (2 µg/ml). The selection pressure was maintained over a period of 12 to 15 days. For the experiments, polyclonal cells were used.

4.2.3. Transfection of A498 cells using Lipofectamine 2000 Transfection Reagent

A498 cells were seeded in 6-well plates and weaned over five days to serum-free media or cultivated media containing 10% FBS. At 80% confluence cells were transfected with 1.25µg, 2.5µg and 5µg of the plasmid either containing the overexpression vector or an empty vector using Lipofectamine 2000 Transfection Reagent according to manufacturer's protocol. Transfection occurred in medium without serum or antibiotics. 4 hours after transfection the medium was changed to culture medium containing FBS.

4.2.4. Transfection of A498 cells using GeneJuice®

A498 cells were seeded in 6-well plates 24 hours before transfection. At 80% confluency cells were transfected with 1, 2 or 4µg of the plasmid either containing the overexpression vector or an empty vector using GeneJuice® according to the manufacturer's protocol.

4.2.5. Transfection of A498 cells using Nucleofector™

A498 cells were cultivated until needed number was achieved. Transfection was performed according to manufacturer's protocol.

4.2.6. Serum starvation of A498 cells

A498 cells were seeded in 12-well plates in medium containing 10% FBS. At 70% confluency medium was changed to medium containing 10, 5, 2.5 or 0% FBS. Pictures were made at 0, 24 and 48 hours after change of medium with a total magnification of 40x.

4.2.7. Lipofectamine 2000 Transfection Reagent gradient with A498 cells

A498 cells were seeded in 24-well plates and weaned gradually to a serum-free medium over five days. Then 2, 3, 4 or 5µL/mL of Lipofectamine 2000 Transfection Reagent were added. Following the manufacturer's protocol medium was changed after 4 hours of incubation at 37°C and 5% CO_2 to medium containing 10% FBS. Pictures were made at 0, 24, 48 and 72 hours after medium change.

4.2.8. Kinome assay

For kinome analyses the commercially available microarray chips for tyrosine (PTK) and serine/threonine kinase (STK) assays from PamGene International B.V. ('s-Hertogenbosch, Netherlands). The PTK PamChip® contains 196 peptide sequences whereas the STK PamChip® contains 144, with each peptide sequence harboring phosphorylation sites for the respective group of kinases.

For the kinase assay, analysis was performed on three biological replicates with pooling of at least three technical replicates each. For cell lysis M-PER buffer supplemented with 10x PhosSTOP and 25x cOmplete Protease Inhibitor Cocktail were added to the cell pellet. The suspension was homogenized using a 20-gauge (0.9mm) needle. After incubation for 1 hour on a rotation shaker at 4°C, lysates were centrifuged at 16,000g for 15 minutes at 4°C. Then the supernatant was collected and aliquoted and transferred to a -80°C freezer for long-time storage. Protein concentration was quantified using the Pierce™ Coomassie Plus (Bradford) Assay Kit according to manufacturer's protocol. Phosphorylation activity of kinases was visualized by fluorescently labelled anti-phospho antibodies and signal intensity was analyzed using the BioNavigator® software.

An upstream kinase tool was used to generate a putative list of kinases responsible for phosphorylating the phosphates on the PamChip. It is an interpretation and is highly dependent on the contents of the underlying phosphorylation databases. Later, the findings are compared with multiple databases such as Human Protein Reference Database[74,75], Reactome[76], UniProt[77], and Phosphosite[78] therefore it becomes possible to identify the active kinases within the sample.

A Kinase score plot is then generated through the BioNavigator Software tool enabling the visualization and identification of the specific kinases.

4.2.9. Western Blot analysis

To analyze protein levels, cell lysates were used to perform a sodium dodecyl sulfate polyacrylamide gel electrophoresis (SDS-PAGE) and western blot. For cell lysis, cell pellets were washed twice with DPBS, resuspended in Lysis buffer, supplemented with 10x

PhosSTOP and 25x cOmplete Protease Inhibitor Cocktail, and sonicated for 1-2 seconds. After that samples were centrifuged at 4°C and 16,000 x g for 20 minutes, followed by determination of protein concentration by a bicinchoninic acid (BCA) assay. For SDS-PAGE, 20µg of total protein were heated at 95°C for 5 minutes in Laemmli buffer and then loaded on a 10% polyacrylamide gel. Samples and standards were separated at 120V for 60-100 minutes using the Mini-PROTEAN® Tetra Cell Systems (Biorad) and then transferred to a PVDF membrane (GE Healthcare Europe GmbH) at 25V for 40 minutes. This was followed by blocking of the membrane for 1 hour using TBST containing 5% non-fat dry milk powder. Membranes were incubated overnight with respective primary antibody (see table 3) at 4°C and afterwards repeatedly washed with TBST. After incubation of membranes with equivalent HRP – linked secondary antibody, Pierce® ECL Western Blotting Substrate and SuperSignal™ West Femto Maximum Sensitivity Substrate were used to visualize protein bands under the ChemiDoc™ MP Imaging System. Results were quantified through the LabImage1D Software.

4.2.10. Histological analysis

Hematoxylin and eosin (HE) stained slides were assessed using the IX51 Inverted Microscope (Olympus). For quantification of mitotic figures, giant cells and Ki-67 proliferation ratio, five random and unconnected fields of view at a total magnification of 400x were counted and evaluated. To analyze the number of tumor nodules and the tumor or metastasis incidence 1 or 5 slides were checked for tumor tissue at a total magnification of 40 – 400x. All results were validated by Prof. Dr. Jochen Fries (Institute for Pathology, University Hospital of Cologne).

4.2.11. Microarray with 786-O cells

The following procedures were performed by Janis Neumann, member of RG Mathieu Clément-Ziza, CMMC Cologne. The statistical data and functional annotation analysis was performed by the author.

Sample collection for microarrays

For the microarray, analysis was performed on three biological replicates (passage three, five and seven) with pooling of at least three technical replicates each. To remove FCS traces, 786-O cells were washed with PBS and then trypsinized (0.05%) for five minutes. The cells were then moved into a 15mL Falcon® tube and centrifuged at 1000RPM for five minutes. After disposal of the supernatant, the cell pellet was washed three times with 3mL PBS. Then, 1mL QIAzol lysis reagent was added and after transfer to a sterile nuclease free tube, samples were sonicated for 30 seconds on ice. Sonicated samples were stored at -80°C until RNA isolation.

RNA isolation

RNA isolation was conducted using miRNeasy® Mini Kit following the manufacturer's protocol. After thawing on ice, samples were triturated on the tube wall through a 24G needle and a 1mL syringe. Then, 200µL chloroform were added to the tube and vortexed shortly before samples were centrifuged at 12,000xg for 15 minutes at 4°C. After precise collection of the upper phase, samples were transferred into 1.5mL nuclease free tubes. Equal volume of pre-chilled 70% ethanol was added and the tube contents were mixed by repeated pipetting. After that, 700µL of the sample were moved into the mini spin column in a 2mL collection tube and centrifuged at 12,000xg for 20 second at RT. This step was then repeated with the retentate. 350µL of RW1 buffer were added to the final retentate in the mini spin column and again centrifuged at 12,000xg at RT. The filtrate was then discarded and 10µl of DNAse and 70µL of RDD buffer were added and the column was incubated for 15 minutes at RT. After washing the column twice with 500µL of RPE wash buffer, it was placed into nuclease free 1.5mL tubes. To elute the RNA, 22µL of nuclease free water were added and the column centrifuged at 12,000xg for 1 minute at RT. After carefully removing the collection tube, it was placed on ice. Using the NanoDrop™ RNA was quantified and the samples were diluted with nuclease free water to reach a final concentration of 33.3ng/µL.

RNA target preparation

With the GeneChip 3´ IVT Express Kit total isolated RNA from the samples is subject to reverse transcription to synthesize first strand complementary DNA (cDNA), which is then converted to double-stranded DNA (dsDNA), serving as a template for transcription. Through in vitro transcription (IVT) complementary RNA (cRNA), with incorporated biotin-conjugated nucleotides, is synthesized. After purification and fragmentation cRNA is hybridized onto GeneChip™ Human Genome U133 Plus 2.0 array.

Poly-A RNA control preparation

First, Poly-A control dilution buffer was pipetted into four nuclease free tubes following table 9. To the first tube 2µL of Poly-A control stock was added, vortexed and spun down before transferring 2µL serially up to tube number 3. To tube number 4, 2µL of the solution from tube number 3 were added. Then 2µL of the solution of tube number 4 were added to 100ng of total RNA from each sample in individual PCR tubes and kept on ice. These were used as RNA/Poly-A RNA controls.

Name	**Poly-A control dilution buffer**	**Poly-A control stock**	**Total volume**	**Dilution**

Tube 1	38µL	2µL	40µL	1:20
Tube 2	98µL	2µL from tube 1	100µL	1:100
Tube 3	98µL	2µL from tube 2	100µL	1:200
Tube 4	18µL	2µLfrom tube 3	20µL	1:2000

Table 9: Scheme for the preparation of Poly-A control tubes.

Synthesis of first- and second-strand cDNA

All reagents needed for the first-strand synthesis were thawed on ice. To prepare the first-strand master mix, 10.5µL of first-strand enzyme mix were added to 42µL of first-strand buffer mix in nuclease free tubes on ice. 5µL of this master mix were then transferred to the individual PCR tubes containing the RNA/Poly-A RNA control mixture. Tubes were carefully vortexed and centrifuged for five seconds and placed on ice. Then PCR tubes were incubated in a thermal cycler for 2 hours a 42°C. Following incubation, tubes were centrifuged briefly and stored on ice. After thawing the reagents for second-strand synthesis on ice, the master mix was prepared. To a nuclease free tube on ice, 52.2µL second-strand buffer mix, 21µL second-strand enzyme mix and 136.5µL of nuclease free water, were added. The mix was vortexed, centrifuged for 5 seconds and placed on ice. To each tube of first-strand cDNA samples 20µL of second-strand master mix were transferred, followed by centrifugation for 5 seconds and storage on ice. After that, PCR tubes were incubated in a thermal cycler block at 16°C for 1 hour, followed by 65°C for 10 minutes and in the end 4°C for at least 2 minutes. Directly after, PCR tubes were briefly centrifuged and placed on ice.

Synthesis of labeled cRNA through in vitro transcription (IVT)

Reagents needed for the IVT master mix were thawed on ice (IVT enzyme mix) or at room temperature (IVT biotin label and labeling buffer). To prepare the master mix, 42µL IVT biotin label, 210µL IVT labeling buffer and 63µL IVT enzyme mix were added to a nuclease free tube at RT. This was followed by gently vortexing and briefly centrifuging the mix, before placing it on ice. To each tube of second-strand cDNA samples, 30µL of this IVT master mix were transferred. All tubes were gently vortexed, briefly centrifuged and then stored on ice. For labeled cRNA synthesis, PCR tubes were placed in a thermal cycler for 16h at 40°C. After incubation, cRNA samples were put on ice immediately.

Purification and fragmentation of cRNA

In preparation of purification, 550µL of cRNA Elution Solution in a RNase free tube were preheated at 50-60°C for 10 minutes. To prepare the cRNA Binding Mix, 110µL of cRNA Binding Beads as well as 550µL cRNA Binding Buffer Concentrate were mixed in a nuclease free tube at RT. To each sample, 60µL of the cRNA Binding Mix were added and then the

samples were transferred to individual wells of a U-Bottom Plate. This was followed by the addition of 120µL of 100% ethanol per sample and gentle mixing through pipetting.
The plate was then placed on a plate shaker and shaken at low velocity (Lab-line titer plate shaker setting 4) for 3 minutes before being moved to a magnetic stand for 5 minutes. When the mixture turned transparent and the cRNA binding beads accumulated in the center of the well, the supernatant was gently removed and discarded. For washing, 100µL of cRNA wash solution were added to each well and mixed gently by pipetting up and down. The plate was then shaken at Lab-line titer plate shaker setting 7 (medium velocity) on the plate shaker for 1 minute. Again, this was followed by placement of the plate on a magnetic stand for 5 minutes. After that, the aforementioned washing process was repeated.
After the last washing step, the plate was shaken at high velocity on the plate shaker (Lab-line titer plate shaker setting 10) for 1 minute. Before shaking for another 5 minutes, 27µL of preheated cRNA elution solution were added to each sample. This was followed by placing the plate on a magnetic stand for 5 minutes. Once again, the cRNA binding beads accumulated in the center and the purified eluted cRNA remained in the supernatant. This supernatant was then aspirated carefully and transferred to nuclease-free tubes and put on ice. Next a spectrophotometer was used to quantify cRNA and then the samples were diluted with nuclease-free water to reach a final concentration of 15µg/32µL. To each sample 8µL of 3´ Fragmentation Buffer were transferred to 32µL (15µg) of cRNA sample in a nuclease-free tube before gently vortexing the tube. In the next step, all samples were incubated in a thermal cycler at 94°C for 35 minutes and then at 4°C for 2 minutes. Immediately after incubation all samples were centrifuged briefly and put on ice.

Hybridization

All needed components were thawed at room temperature. First, the 20X Hybridization Controls were heated at 65°C for 5 minutes. To prepare the Hybridization Master Mix, 42µL of 3nM Control Oligo™ B2, 125µL of 20X Hybridization Control, 1.25µL of 2X Hybridization Mix and 250µL of DMSO were added to a nuclease-free tube. To each one of 10 nuclease-free tubes 166.7µL of hybridization master mix was transferred. After addition of 50µL of nuclease-free water to each tube, 33.3µL (12.5ng) of fragmented labeled cRNA was added to the respective tubes. These hybridization cocktails were gently vortexed and then centrifuged briefly.
In preparation for the hybridization, the probe array was equilibrated at RT for at least 30 minutes. To prehybridize the array, a pipette tip was inserted in the upper right septum for venting purposes, while 200µL of the Pre-Hybridization Mix were filled through the left bottom septum. This was followed by the removal of the pipette tip from the upper right septum and incubation of the array with a rotation at 60rpm for 10-30 minutes at 45°C.

Then the tubes containing the hybridization cocktail were incubated for 5 minutes at 99°C, followed by 5 minutes at 45°C in a heat block. The array was removed from the hybridization oven, vented with another pipette tip and the Pre-Hybridization Mix was removed. After that, the array was refilled with 200µL of the Hybridization Cocktail and both septa were covered with Tough-Spots™. Then the array was incubated for 16 hours at 45°C and rotation at 60rpm.

Washing, staining and scanning of the GeneChip™ array

After removal of the array from the hybridization oven and of the Tough-Spots™ from the septa, the Hybridization Cocktail mix was removed. This was followed by filling the array with Wash Buffer A and continued by washing and staining following the protocol enclosed to the GeneChip™ Fluidics Station 450. GeneChip™ Scanner 3000-7G was used to scan the stained arrays and the GeneChip™ operating software was used for quality control analysis.

Statistical data and functional annotation analysis

The obtained .cel files from the arrays were uploaded in Partek® Genomics Suite® (PGS) version 6.6 for statistical analyses. To create suitable data set for further statistical analysis the RMA (Robust Multichip Average) model was used. The model included the steps of background correction, log2 transformation, quantile normalization and median polished probe normalization. These data sets were then subjected to principal component analysis (PCA) and a one-way ANOVA model to bring out transcripts, that are differentially expressed with a minimum of a 2-fold change. The generated data sets were then normalized by Z score and the differentially expressed transcripts were clustered through a hierarchical cluster analysis (PGS). The collectively differentially expressed transcripts were created via generating Venn diagrams (PGS). For functional annotation and gene ontology clustering of differentially expressed transcripts the free online software DAVID (Database for Annotation, Visualisation and Integrated Discovery) was used[79,80]. CellNet[81],the open access software tool, was used to identify the cellular identity through the transcription profile.

4.2.12. Statistical analysis

Statistical analyses were performed using the GraphPad Prism 10 software. Histological data was analyzed through ordinary one-way ANOVA, followed by Tukey's multiple comparisons as a post-hoc test. P values less than 0.05 were considered statistically significant.

5. Results

5.1 Overexpression of NEDD9 in A498 cells

NEDD9 is known to increase tumor invasion and metastasis in several tumor entities including breast cancer, NSCLC, melanoma, colorectal cancer and prostate cancer[55,66]. In RCC, NEDD9 expression was associated with higher tumor stage as well as lower overall survival[63]. In human ccRCC cell lines 786-O and Caki1, migration and invasion were found to be decreased in response to NEDD9 downregulation[63]. Here, we choose another human ccRCC cell line, namely A498 which endogenously expresses low levels of NEDD9 and aimed to overexpress NEDD9 to subsequently analyze the influence of low versus high NEDD9 expression levels on cellular processes such as migration, proliferation and invasion. Therefore, we transfected A498 cells with a plasmid containing either an overexpression vector for NEDD9 or an empty vector. The plasmid contained full-length NEDD9 cDNA with the 834 amino-acid sequence from Law et al.[82] This sequence is located in a *Eco*Ri-*Xho*I-cut pcDNA3 vector, that expresses the protein through a cytomegalovirus promoter. Cells were transfected using Lipofectamine 2000 Transfection Reagent according to established protocols. Unfortunately, the chosen transfection method exhibited repeatedly and constantly high cytotoxicity as almost all cells were found dead and visually floating in medium 24 hours after transfection. The cause of the high cytotoxicity was subsequently analyzed in detail to overcome potential methodological causes.

The cytotoxicity can be caused by different components of the transfection process. In question are 1. the serum-free conditions that are required during the transfection, 2. Lipofectamine 2000 Transfection Reagent and 3. the used overexpression plasmid. To address the first question, A498 cells were incubated with different concentrations of serum, since transfection with Lipofectamine 2000 Transfection Reagent requires serum-free medium. This revealed that A498 cells show high cell death in serum-reduced as well as serum-free conditions. Increased cell death was detected by visual determination of cell density and the number of dead cells floating in the medium (Fig. 3).

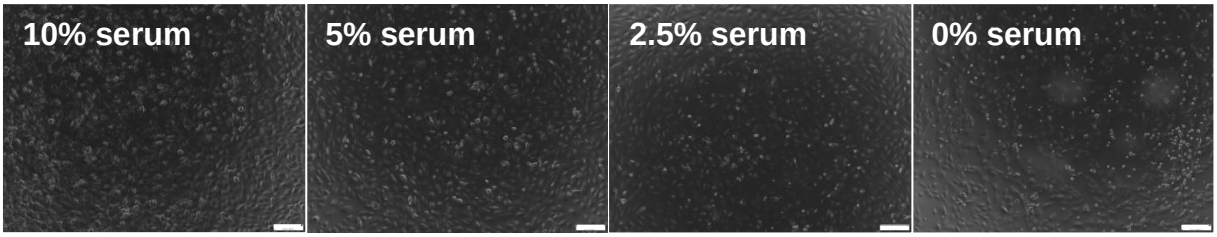

Figure 3: Serum starvation of A498 cells. Representative pictures 24 hours after incubation in culture medium with serum concentrations of 10, 5, 2.5 or 0%. Total magnification of 40x. Scale bar in the bottom right hand corner equals 200µm.

To possibly reduce the reaction to sudden serum withdrawal, A498 cells were gradually weaned. One day after seeding of the cells, the serum concentration in the medium was decreased from 10% to 5%. After three days medium was changed to serum-free medium. One day later, transfection was performed. Nevertheless, the following transfections still showed high cytotoxicity.

To investigate whether Lipofectamine 2000 Transfection Reagent is the reason for the observed cytotoxicity, A498 cells were transfected with different concentrations of Lipofectamine. A498 cells showed high cytotoxicity in the presence of Lipofectamine concentrations as low as 2µL/mL (Fig. 4).

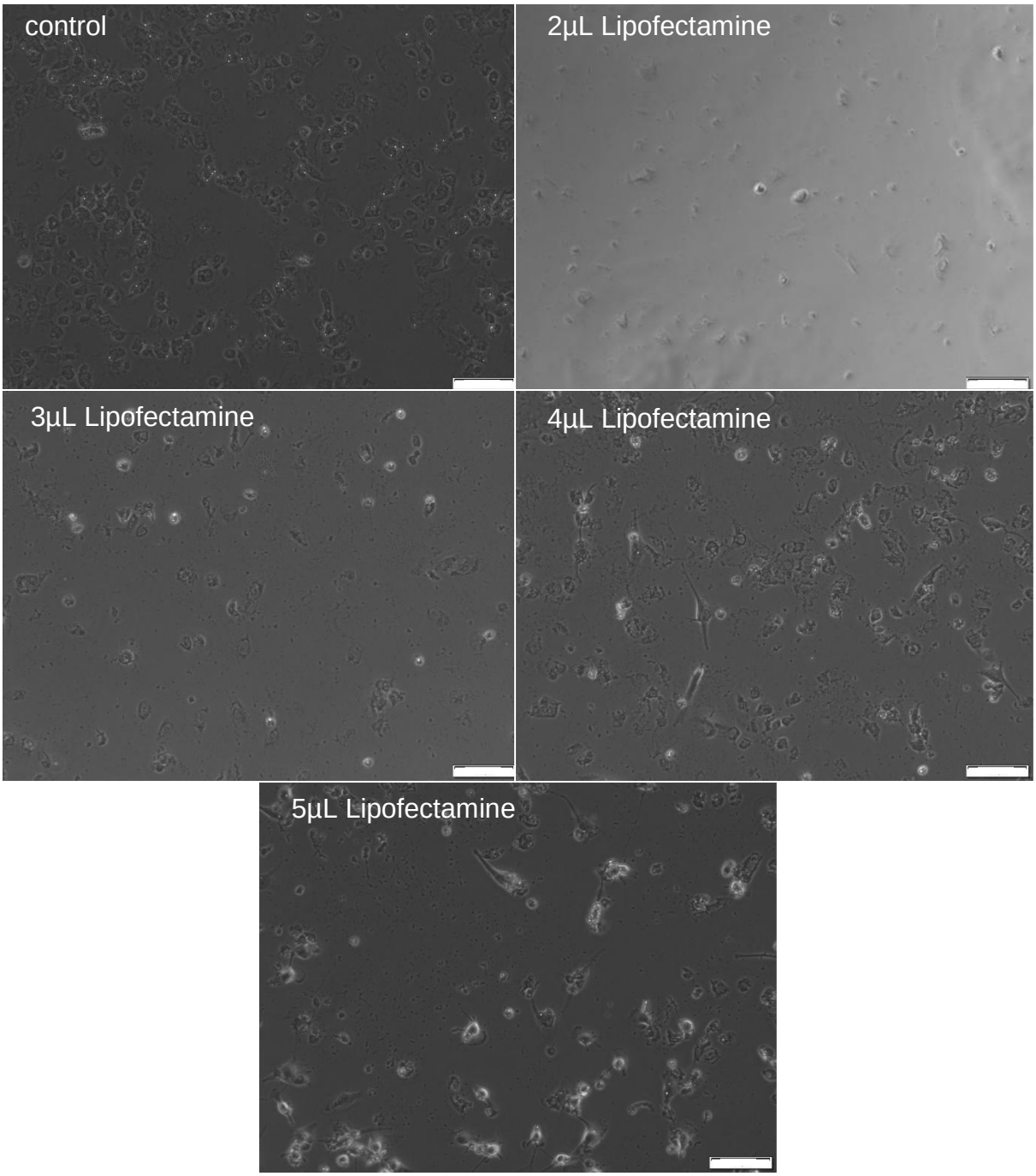

Figure 4: A498 cells with a Lipofectamine 2000 Transfection Reagent gradient. Cells were incubated with Lipofectamine concentrations of either 0, 2, 3, 4 or 5µL/mL medium. Representative pictures 24 hours after incubation. Total magnification of 40x. Scale bar in the bottom right hand corner equals 100µm.

Therefore, we sought another transfection reagent reported to have a low cytotoxicity, namely GeneJuice®. Although the transfections with GeneJuice® showed lesser cytotoxicity compared to transfections with Lipofectamine, the efficiency, as repeatedly tested by Western Blot (Fig. 5 left), was not significant enough to perform further functional assays.

Thus, to overcome this problem, we opted for a third transfection method, namely electroporation using Nucleofector™, which is known to have a high transfection efficiency and low cytotoxicity. Here, transfection experiments showed even lower cytotoxicity than

transfections with GeneJuice®, but also low efficiency (Fig. 5 right), so that further functional assays were not possible.

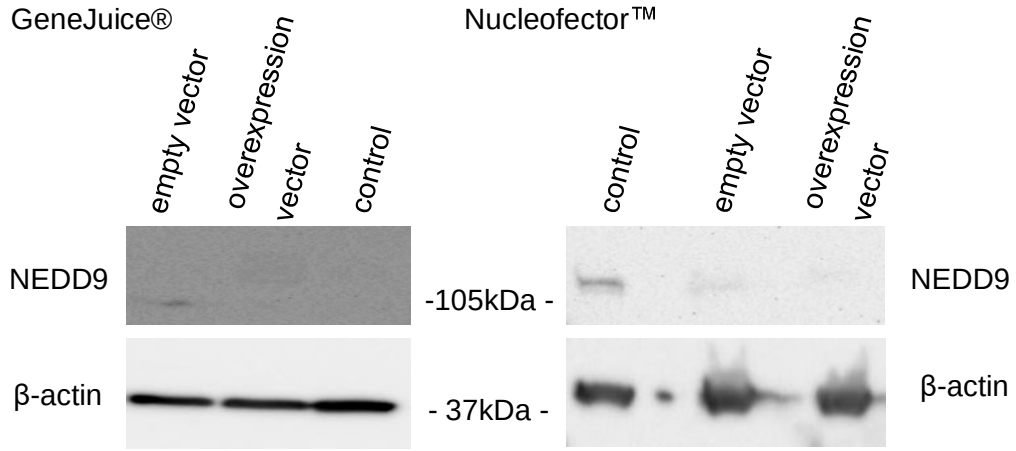

Figure 5: Western Blot for NEDD9 after transfection of A498 cells. Depicted are representative Western Blots for NEDD9 and β-actin as a control after transfection of the overexpression plasmid for NEDD9 using either GeneJuice® (left) or Nucleofector™ (right) as the transfection method.

The transfection methods used differ in their underlying mechanism and in the type of reagent. Both Lipofectamine 2000 and GeneJuice® are chemicals to help transfer the desired transfection vector into the cell, while Nucleofector™ is based on the physical effect of electroporation. Lipofectamine 2000 consists of a cationic lipid designed to form liposomes containing the desired transfection vector. GeneJuice® is a mixture of a cellular protein and a polyamine containing both a positively and negatively charged domain. Together with the negatively charged nucleic acid of the transfection vector, it forms a complex. The nucleic acid-transfection reagent complexes formed by either Lipofectamine 2000 or GeneJuice® are taken up by endocytosis, when they come close to the cell membrane.

The underlying mechanism of electroporation used in the nucleofection technique is still not fully understood. It is believed that the electric pulse ruptures the cell membrane and forms small pores through which the desired transfection vector can enter the cell[83].

Another cause for the inefficient transfections could be the NEDD9 overexpression plasmid itself. This possibility was tested by the positive GFP control in transfections with Nucleofector™, which also showed low transfection efficiency. This led us to the conclusion that the utilized plasmid harboring the NEDD9 overexpression vector could play a role in the observed low efficiency. Therefore, we planned to repeat the experiments with a newly designed overexpression vector under the control of tetracycline. However, this experiment has yet to be performed as the focus of my thesis about the role of NEDD9 in ccRCC pathology shifted to the histopathological evaluation and kinome analysis of previously performed mouse experiments.

5.2 Histological analyses of syngeneic and xenograft mouse models

To investigate the role of NEDD9 in RCC *in vivo,* two different mouse models were generated and tested by Mariia Cherviakova in her dissertation which was successfully completed within the same working group[72].

NEDD9- competent and -deficient 786-O and Renca cells were generated through lentiviral transfection of small hairpin RNA (shRNA). Two small hairpin RNA per cell line (shC and shD in 786-O, shA and shB in Renca cells) interfering with NEDD9 mRNA and one small hairpin RNA with an empty control (nontargeted) vector (shNT) were transfected. Depletion of NEDD9 was controlled on protein level via Western Blot (Fig. 6).

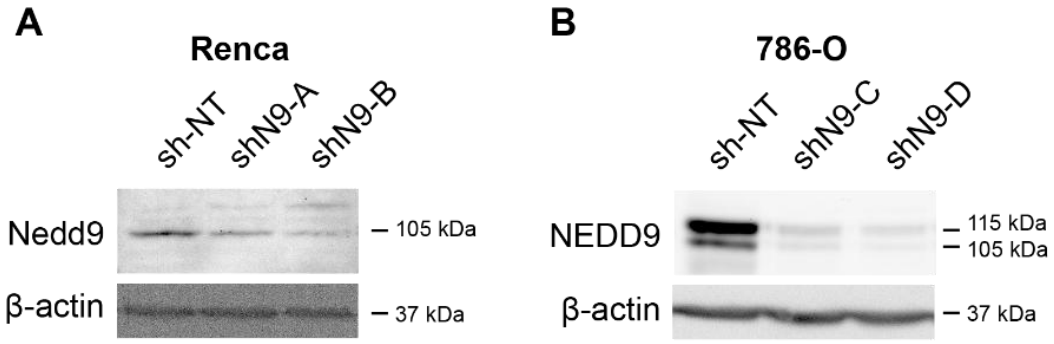

Figure 6: NEDD9 knockdown by shRNA in human and murine RCC cells in vitro. A and B: Representative blots of murine (A, Renca) and human RCC cell line (B, 786-O) cells after lentiviral transfection. Cells were lysed in RIPA-Buffer and NEDD9 protein expression was detected by Western blot analysis. Western Blot courtesy of AG Dr. med. Tamina Seeger-Nukpezah.

The first mouse model is a syngeneic mouse model in which murine NEDD9-competent and NEDD9-deficient Renca cells were injected into Balb/c mice, which are of the same genetic background as Renca cells. The second mouse model is a xenograft mouse model in which human NEDD9-competent and NEDD9-deficient 786-O cells were injected in NOD (Non-obese diabetic) SCID (severe combined immunodeficiency) gamma (NSG) mice (Fig. 7). In both mouse models, tumor cells were either injected subcutaneously into the left flank or orthotopically under the renal capsule to mimic a more authentic tumor environment. At the end of each experiment or when the mice reached the termination criterion, mice were euthanized and the tumors/ tumor-bearing kidneys as well as the organs most frequently affected by metastasis, namely liver and lung, were harvested for further histological analysis.

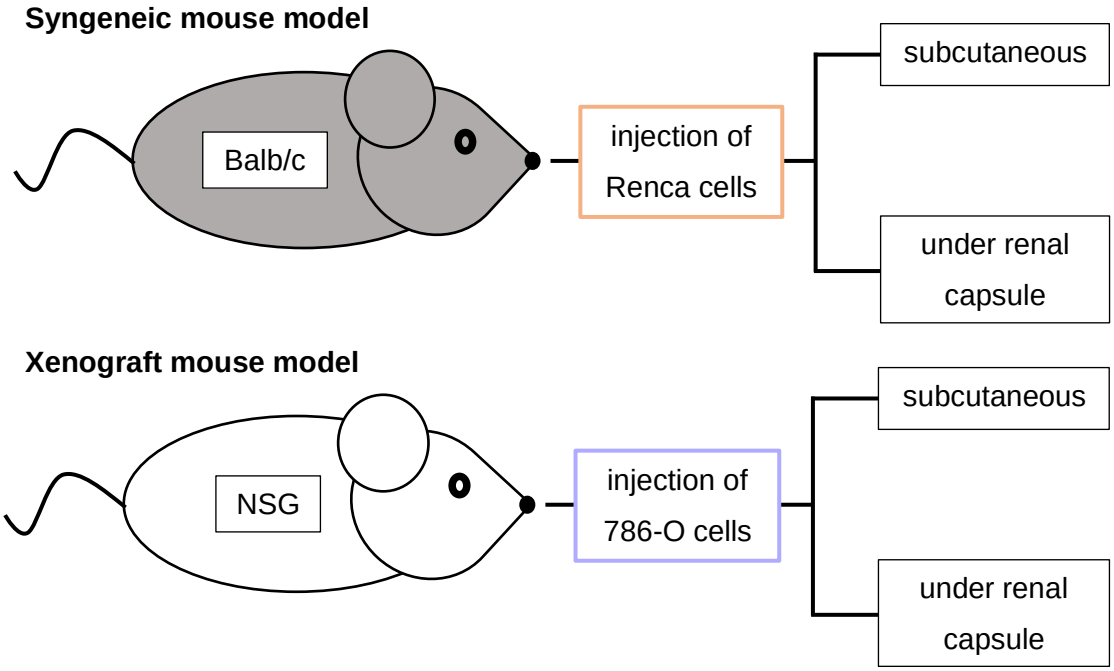

Figure 7: Schematic depiction of the different mouse models. Upper range: syngeneic mouse model with murine Renca cells injected into Balb/c mice. Lower range: xenograft mouse model with human 786-O cells injected into NSG mice. In both mouse models, injections of the respective cells were performed subcutaneously and orthotopically under the renal capsule.

Histological analyses included evaluation of tumor nodules and tumor area, number of mitotic figures and giant cells as well as metastasis incidence and the number of metastatic nodules in hematoxylin and eosin (HE) stained slides. In addition, possible effects of NEDD9 on proliferation and apoptosis was conducted by analyzing slides with Ki-67 and caspase-3 staining respectively.

HE stained slides (Fig. 8) of kidney, lung, liver and primary tumor were completely scanned for tumor tissue. To evaluate the number of giant cells and mitotic figures (Fig. 9), five non-contiguous fields of view (FOV) within tumor tissue were chosen for quantification. Likewise, in Ki-67-stained slides five non-contiguous fields of view within tumor tissue were chosen for analysis.

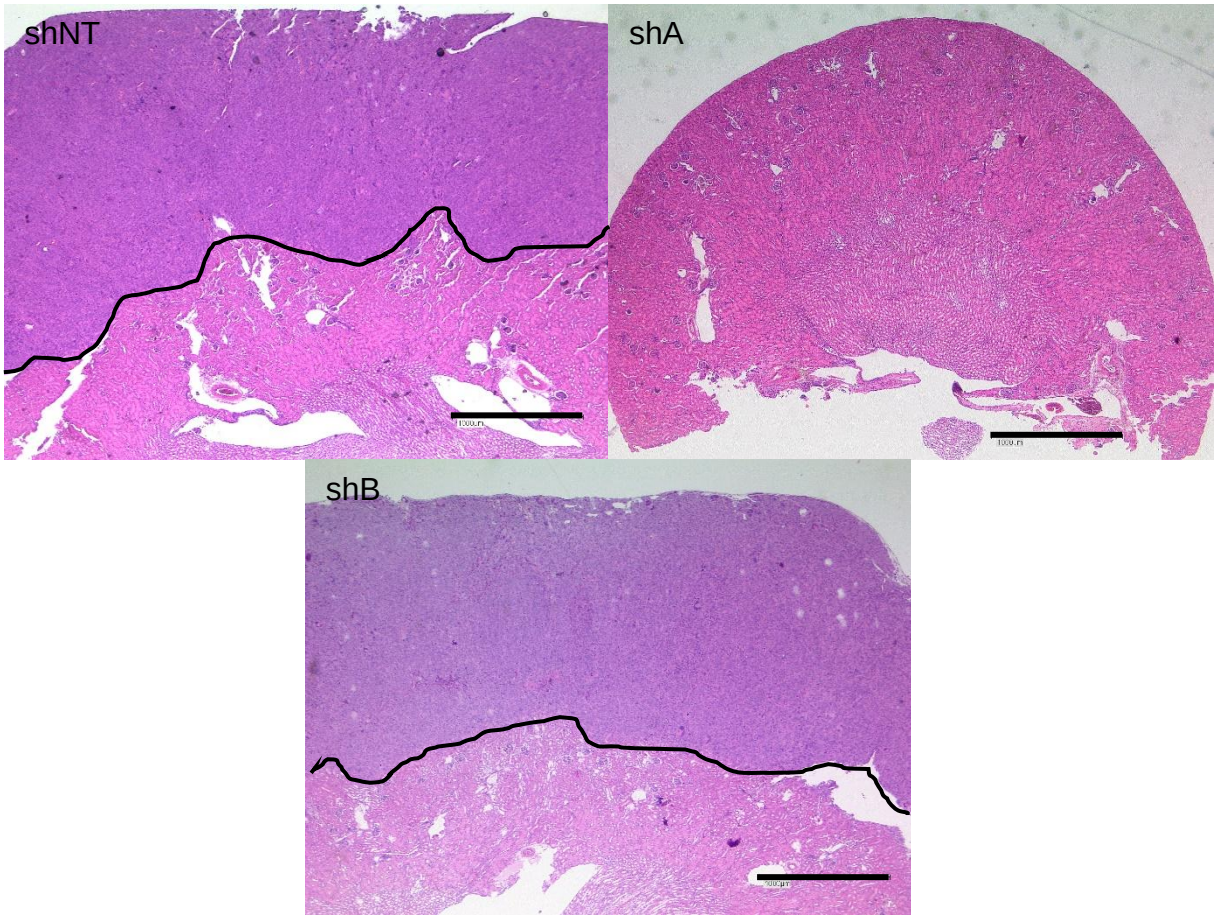

Figure 8: Representative images of kidney sections of the syngeneic mouse model after orthotopic injection of murine Renca cells. Kidney sections were HE stained and microscopic images were taken at total magnification of 2.5x. Tumor tissue lies above the black line in shNT and shB. Scale bar equals 1000µm.

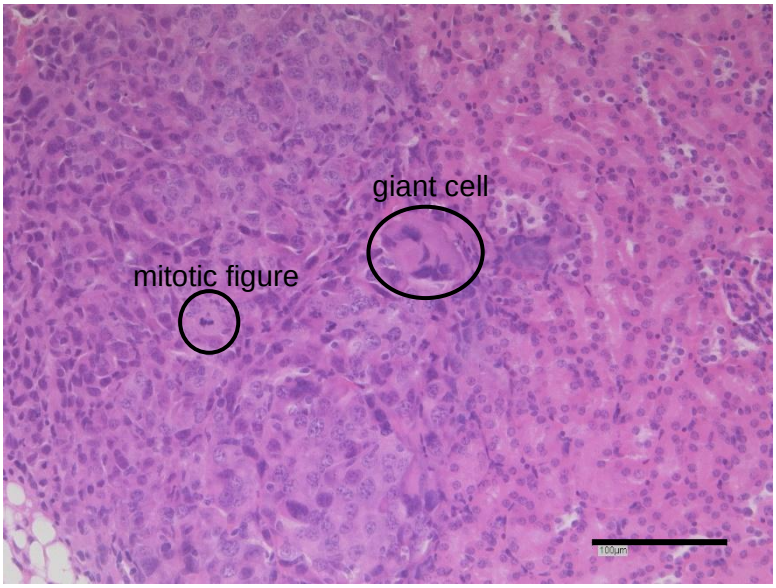

Figure 9: Representative picture of a giant cell and a mitotic figure. HE-stained slide of normal kidney tissue and adjacent tumor tissue from the syngeneic mouse model after injection of NEDD9-competent Renca cells under the renal capsule at a total magnification of 40x. Scale bar equals 100µm.

In the syngeneic mouse model, murine NEDD9-competent (shNT) and -deficient (shA, shB) Renca cells were injected orthotopically under the renal capsule of Balb/c mice. All animals developed primary tumors at the injection site. In the previous project of Mariia Cherviakova tumor burden was analyzed using MRI imaging and tumor weight. Here, a significant increase in tumor weight (shNT vs shA $p \leq 0.05$, shNT vs shB $p \leq 0.01$) as well as tumor volume (shNT vs shA/B $p \leq 0.01$) could be seen in NEDD9-competent tumors in comparison to NEDD9-deficient tumors (Fig. 10)[72].

The focus of this project was to analyze above mentioned histological features and signaling of NEDD9-deficient versus -competent tumors rather than quantifying total tumor burden.

In this experiment, nine mice were orthotopically injected with NEDD9-competent shNT Renca cells in the control group and eight and nine mice with NEDD9-deficient shA and shB Renca cells for the test group respectively. First, a histological section was made through each tumor bearing kidney and stained with HE. The ratio of tumor area to normal kidney tissue and the number of tumor nodules were comparable between groups in this single section. This single section was not suitable for quantification of total tumor burden, but was used to analyze the histological characteristics within the tumor tissue arising from NEDD9-competent compared to NEDD9-deficient cells (Fig. 11).

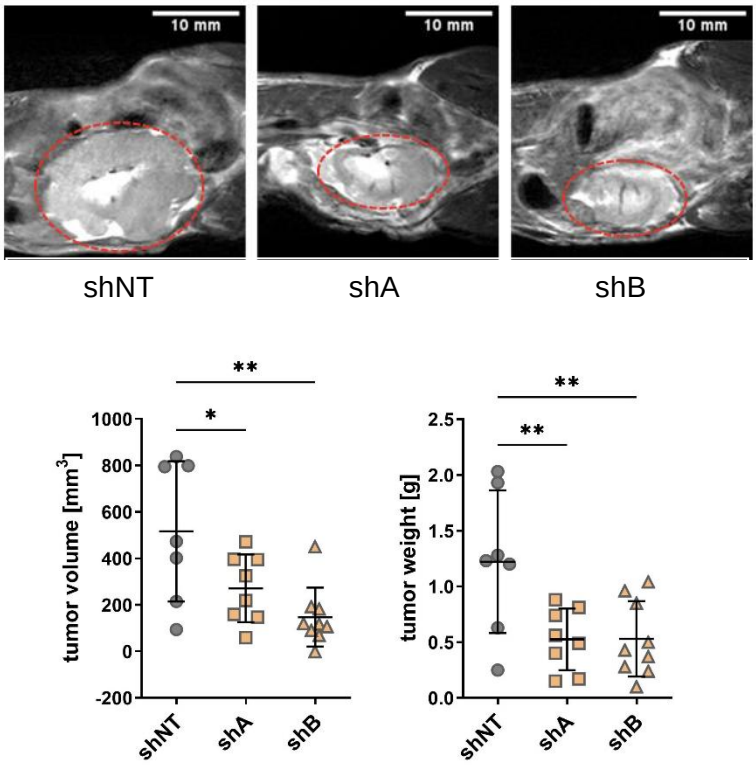

Figure 10: Quantification of total tumor burden in the syngeneic mouse model after orthotopic injection of NEDD9-competent or -deficient murine Renca cells. Top: representative MRI scans of the abdomen of mice on day 16 after orthotopic injection of NEDD9-competent (shNT) or -deficient (shA/shB) murine Renca cells. Kidneys are marked by red oval. Bottom left: MRI-based quantification of total tumor volume. Bottom right: Quantification of tumor weight post mortem. Statistical analysis was performed through ordinary one-way ANOVA. * $p \leq 0.05$, ** $p \leq 0.01$ Data are expressed as +/- SD. shNT n=9 mice, shA n=8 mice, shB n=9 mice. Adapted from Cherviakova[72]

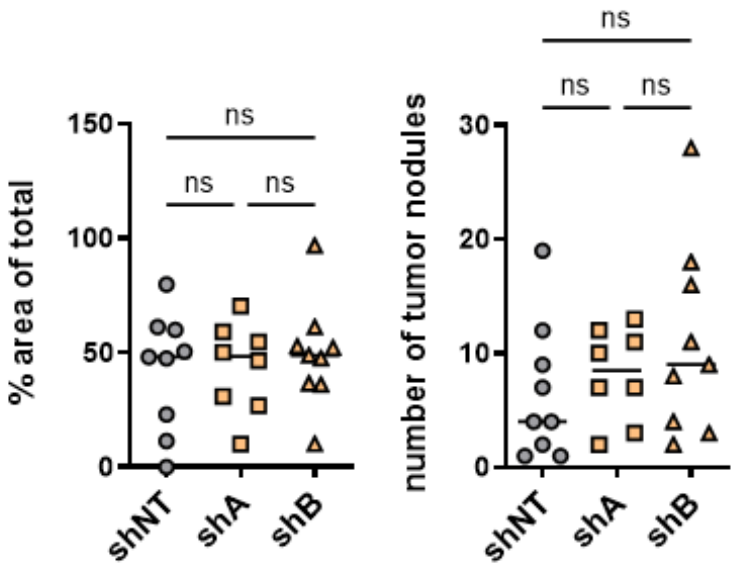

Figure 11: Histological analysis of renal tumors of the syngeneic mouse model after orthotopic injection of NEDD9-competent or -deficient murine Renca cells. Analysis of the number of tumor nodules (left) and the percentage of tumor area to total area (right). Statistical analysis was performed through ordinary one-way ANOVA. ns=not significant. Data are expressed as +/-SD. shNT n=9 mice, shA n=8 mice, shB n=9 mice

To characterize the tumor further, mitotic figures and giant cells were counted, indicating increased cell division and incomplete cell differentiation[84,85]. Tumors with less differentiated cells are associated with a poor prognosis and giant cells are associated with aggressive RCC and predicted to have a role in the development of drug resistance[21,85,86]. The number of mitotic figures was significantly higher in NEDD9-competent than in NEDD9-deficient tumors (shNT vs. shA p=0.0001, shNT vs. shB p=0.0164), while the number of giant cells showed no significant difference (Fig. 12).

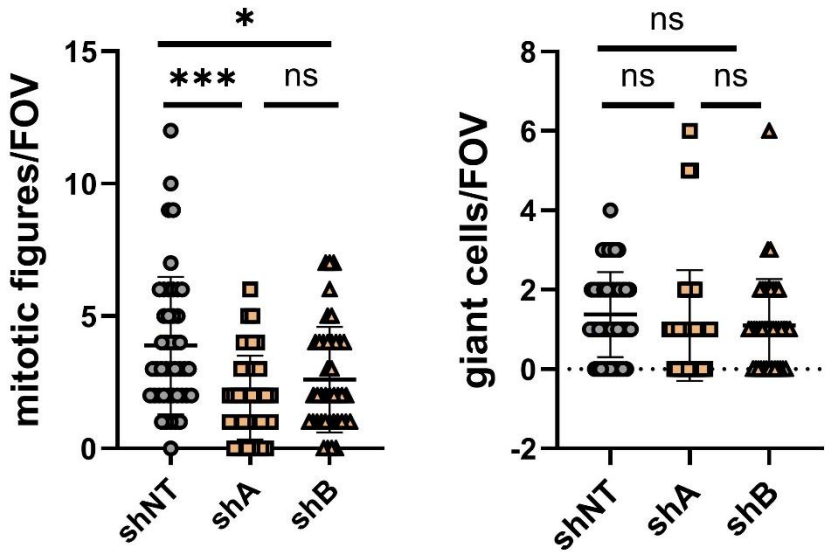

Figure 12: Histological analysis of renal tumors of the syngeneic mouse model after orthotopic injection of NEDD9-competent or -deficient murine Renca cells. Quantification of mitotic figures (left) and giant cells (right). Statistical analysis was performed through ordinary one-way ANOVA. * $p \leq 0.05$, *** $p \leq 0.001$ ns=not significant. Data are expressed as +/- SD. shNT n=9 mice, shA n=8 mice, shB n=9 mice; 5 non-contiguous fields of view per mouse were counted.

To further evaluate the effects of NEDD9 on proliferation, kidney sections of the orthotopic syngeneic mouse model were stained for Ki-67. Ki-67 staining is an established method for distinguishing cells in active phases of the cell cycle, such as G1-, S-, G2- and M-phase, from quiescent cells in G0-phase[87]. The analysis results revealed a striking difference in dependence of NEDD9 expression in RCC tumors (Fig. 13). NEDD9-competent tumors showed a significantly higher proliferation rate than NEDD9-deficient tumors (shNT vs. shA/shB p <0.0001) suggesting that NEDD9 affects the progression in RCC.

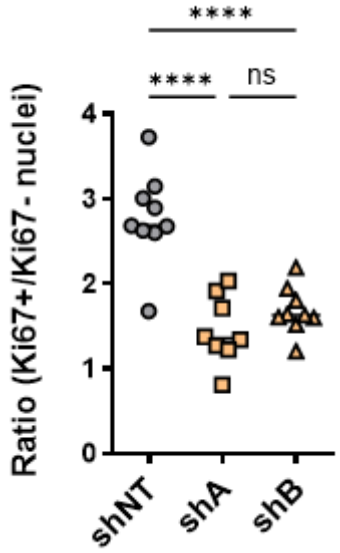

Figure 13: Histological analysis of Ki-67-stained renal tumors of the syngeneic mouse model after orthotopic injection of NEDD9-competent or -deficient murine Renca cells. Ratio of Ki67-positive to -negative cells. Statistical analysis was performed through ordinary one-way ANOVA. **** $p \leq 0.0001$, ns=not significant. Data are expressed as +/- SD. shNT n=9 mice, shB n=9 mice, shA n=8 mice.

To investigate a possible effect of NEDD9 on apoptosis, kidney sections of the orthotopic syngeneic mouse model were stained for caspase-3. Caspase-3 is one of the major effector caspases active during apoptosis[88]. It is at the junction of the extrinsic pathway, triggered by the FAS receptor and the intrinsic pathway, induced by the release of cytochrome c from the mitochondria[89]. Therefore, active caspase-3 is characteristic of cells undergoing cell death. One of the main characteristics of tumor cells is their ability to prevent apoptosis, although they harbor DNA damage and show altered protein expression[90]. However, the expression of NEDD9 had no effect on the expression of caspase 3, indicating that the effect of NEDD9 in RCC is not primarily mediated by apoptosis. Of note, there was no significant difference between NEDD9-competent and -deficient tissue, nor between tumor tissue and normal tissue (Fig. 14).

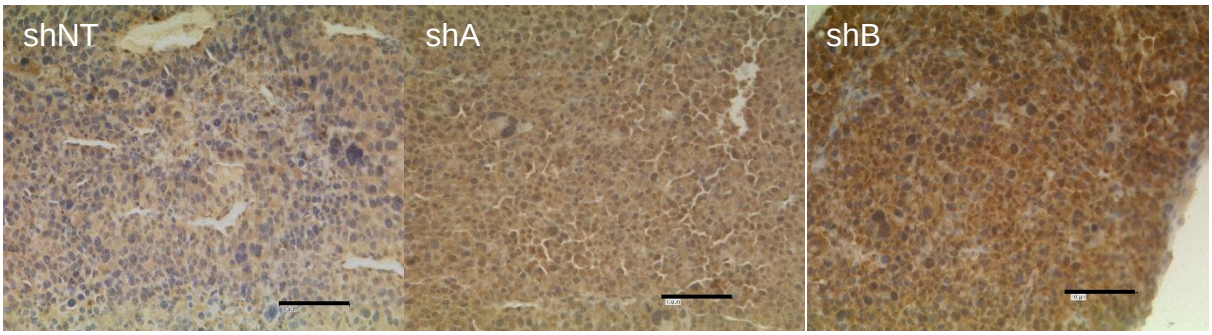

Figure 14: Representative caspase-3 stained of renal tumor sections of the syngeneic mouse model after orthotopic injection of NEDD9-competent or -deficient murine Renca cells. Renal tumor sections were subjected to immunohistochemical staining of caspase-3 and microscopic images were taken at 20x magnification. Scale bar equals 100µm.

One criterium for classifying the extent of spread of cancer is metastasis to distant organs. The most common metastatic sites for RCC include lymph nodes, lung, bones, liver and brain[22]. To

examine a possible effect of NEDD9 on metastasis in RCC, sections of liver and lung were scanned for the presence of tumor tissue after orthotopic injection of tumor cells and, if present, the number of tumor nodules was quantified. As even NEDD9-competent cells rarely metastasized, no significant difference in the frequency and number of metastases to liver (Fig. 15A) and lung (Fig. 15B) was detectable between animals injected with NEDD9-competent and –deficient cells.

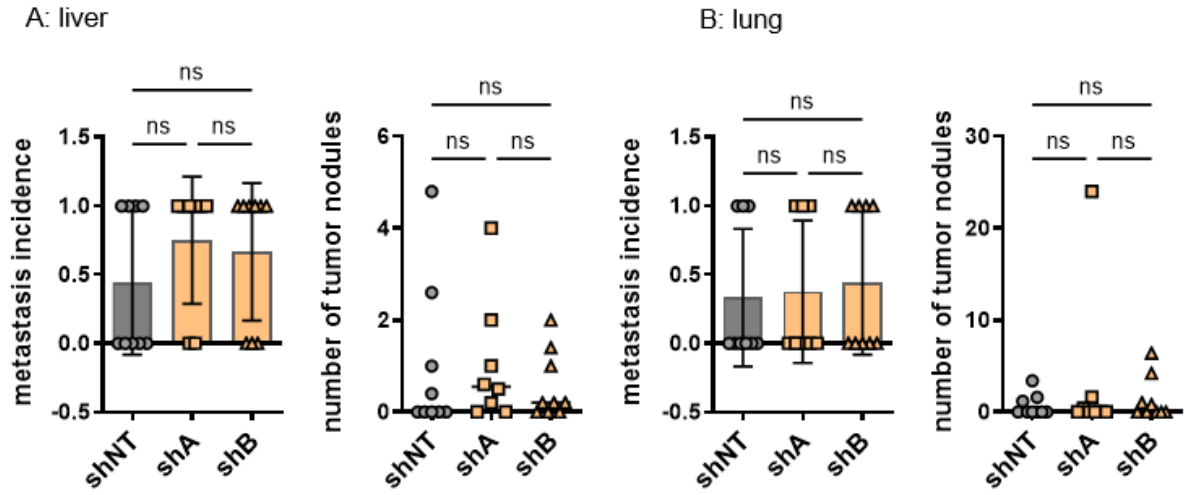

Figure 15: Histological analysis of metastasis to lung and liver in syngeneic mouse model after orthotopic injection of NEDD9-competent or -deficient murine Renca cells. A. Incidence of metastasis and number of tumor nodules in the liver. B. Incidence of metastasis and number of tumor nodules in the lung. Statistical analysis was performed through ordinary one-way ANOVA. ns=not significant. Data are expressed as +/- SD. shNT n=9 mice, shA n=8 mice, shB n=9 mice

In a subcutaneous syngeneic model, murine NEDD9-competent (shNT) and -deficient (shA, shB) Renca cells were injected subcutaneously into the left flank of Balb/c mice. Similar histological analysis regarding the incidence of metastasis and number of tumor nodules in kidney and lung showed no significant difference between animals injected with NEDD9-competent or -deficient tumor cells (Fig. 16). As in the orthotopic syngeneic mouse model, the frequency of metastasis was too low to expect any conclusive result. The tumor incidence of subcutaneous primary tumors was 100% in both groups. However, tumor growth could not be reliably quantified due to very aggressive invasive growth.

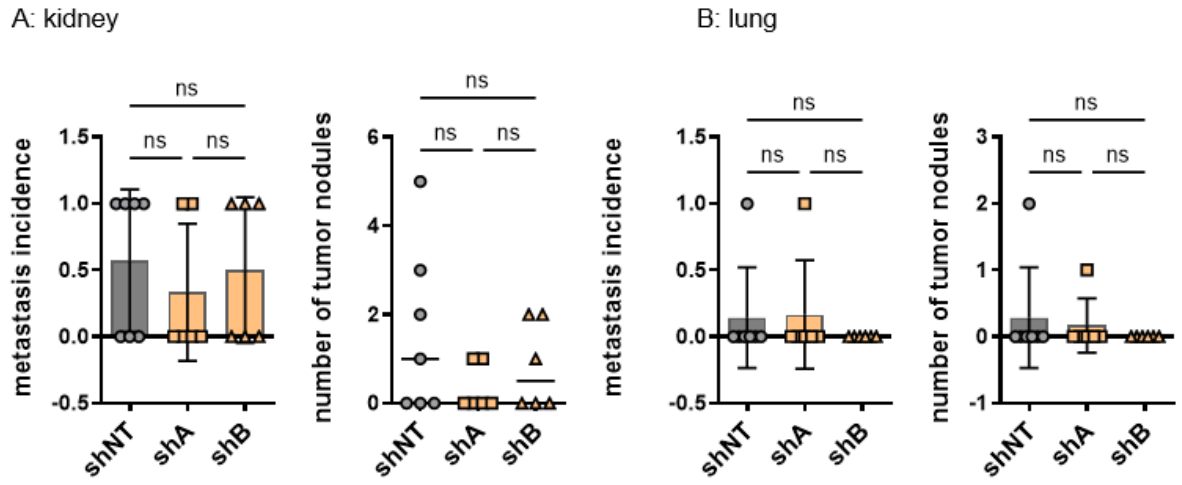

Figure 16: Histological analysis of metastasis to kidney and lung in syngeneic mouse model after subcutaneous injection of NEDD9-competent or -deficient murine Renca cells. A. Incidence of metastasis and number of tumor nodules in the kidney. B. Incidence of metastasis and number of tumor nodules in the lung. Statistical analysis was performed through ordinary one-way ANOVA. ns=not significant. Data are expressed as +/- SD. shNT n=9 mice, shA n=8 mice, shB n=9 mice.

To evaluate the aggressiveness of NEDD9-competent and -deficient tumors, mitotic figures and giant cells were counted (Fig. 17). Here a significant difference in mitotic figures and giant cells could be seen; in NEDD9-deficient tumors the number of mitotic figures (shNT vs. shA p=0.0089, shNT vs. shB p=0.0079) and giant cells (shNT vs. shA p= <0.0001, shNT vs. shB p= <0.0001) was significantly lower compared to NEDD9-competent tumors.

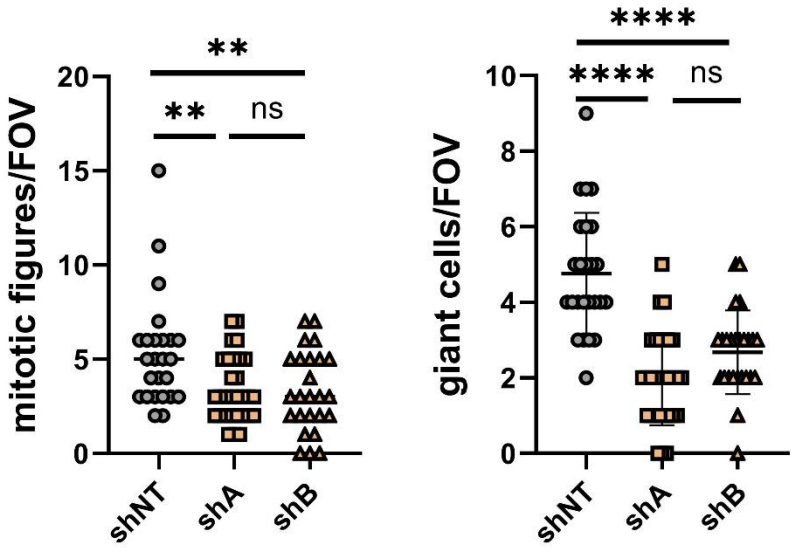

Figure 17: Histological analysis of mitotic figures and giant cells in tumors from syngeneic mouse model after subcutaneous injection of NEDD9-competent or -deficient murine Renca cells. Quantification of the number of mitotic figures (left) and giant cells (right) per field of view (FOV). Statistical analysis was performed through ordinary one-way ANOVA. ** p ≤ 0.01, **** p ≤ 0.0001, ns=not significant. Data are expressed as +/- SD. shNT n=5 mice, shA n=6 mice, shB n=5 mice; 5 non-contiguous fields of view per mouse were counted.

We next examined the impact of NEDD9 in a xenograft mouse model. For this purpose, NEDD9-competent (shNT) and -deficient (shC, shD) human 786-O ccRCC cells were injected in NSG mice orthotopically under the renal capsule. *In vivo,* a significant difference regarding tumor volume (shNT vs shC/D $p \leq 0.05$) as well as tumor weight (shNT vs shC/D $p \leq 0.05$) could be observed when comparing NEDD9-competent to -deficient tumors (Fig. 18)[72]. While in shNT 786-O ccRCC cells formed histologically detectable tumors in 60% of injected mice, only a single tiny tumor grew from the NEDD9-deficient cells. Thus, there was a significant difference between NEDD9-competent and -deficient tumors in terms of tumor incidence (shNT vs. shC p=0.0008, shNT vs. shD p=0.0008), number of tumor nodules (shNT vs. shC p=0.0111, shNT vs. shD p=0.0111) and tumor area relative to total tissue area (shNT vs. shC/shD p=0.0231) (Fig. 19).

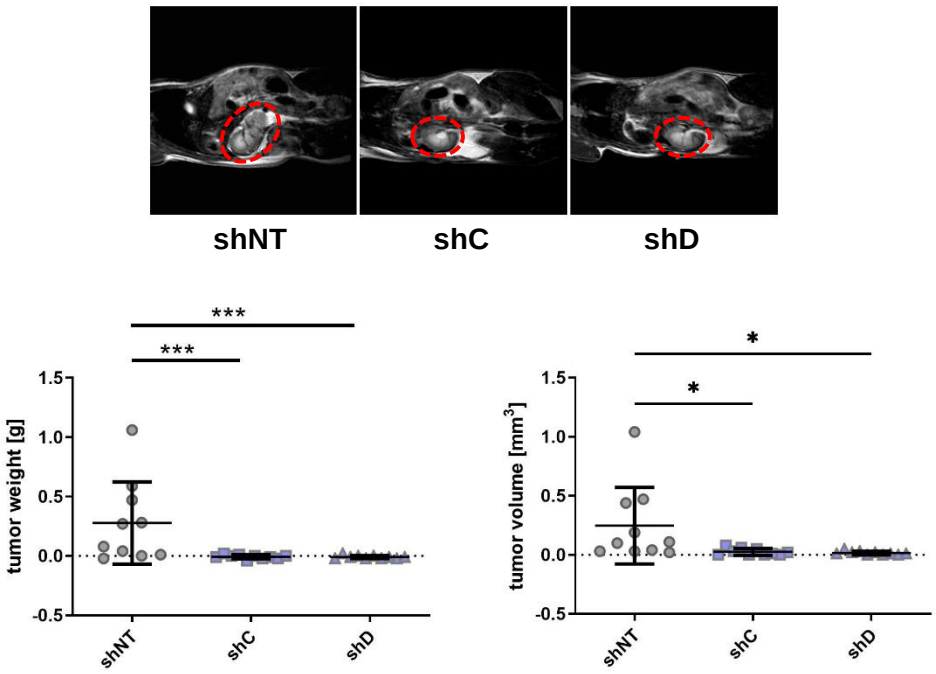

Figure 18: Quantification of total tumor burden in the xenograft mouse model after orthotopic injection of NEDD9-competent or -deficient human 786-O cells. Top: representative MRI scans of the abdomen of mice on day 16 after orthotopic injection of NEDD9-competent (shNT) or -deficient (shC/shD) human 786-O cells. Kidneys are marked by red oval. Bottom left: MRI-based quantification of total tumor volume. shNT n=10 mice, shC n=6 mice, shD n=6 mice. Bottom right: Quantification of tumor weight post mortem. shNT n= 10 mice, shC n=10 mice, shD n=10 mice. Statistical analysis was performed through ordinary one-way ANOVA. * $p \leq 0.05$. Data are expressed as +/- SD. Adapted from Cherviakova[72].

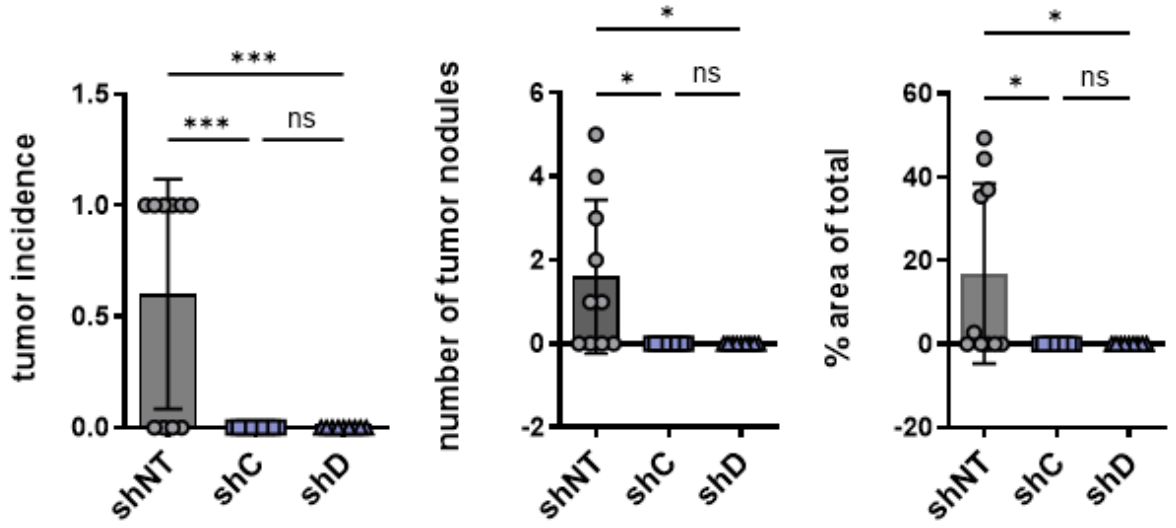

Figure 19: Histological analysis of kidney sections of the xenograft mouse model after orthotopic injection of NEDD9-competent or -deficient human 786-O cells. Analysis of tumor incidence (left), number of tumor nodules (middle) and tumor area to total area (right). Statistical analysis was performed through ordinary one-way ANOVA. * $p \leq 0.05$, *** $p \leq 0.001$, ns=not significant. Data are expressed as +/- SD. shNT n=10 mice, shC and shD n=9 mice.

To evaluate the effect of NEDD9 on metastasis to liver and lung of the orthotopic xenograft models, which are among the most common sites of metastasis in RCC[22], HE-stained slides of those organs were scanned and analyzed for metastasis incidence and number of tumor nodules. Similar to the syngeneic mouse model, metastasis incidence was very low, subsequently a valid statistical analysis was not possible. While in NEDD9-deficient tumors no metastasis was detectable, in the control group only two animals developed detectable metastasis in the lung with an average of 0.2 tumor nodules per five slides (Fig. 20). For the same reason, statistical analysis of the quantification of mitotic figures, giant cells and proliferation marker Ki-67 was not possible.

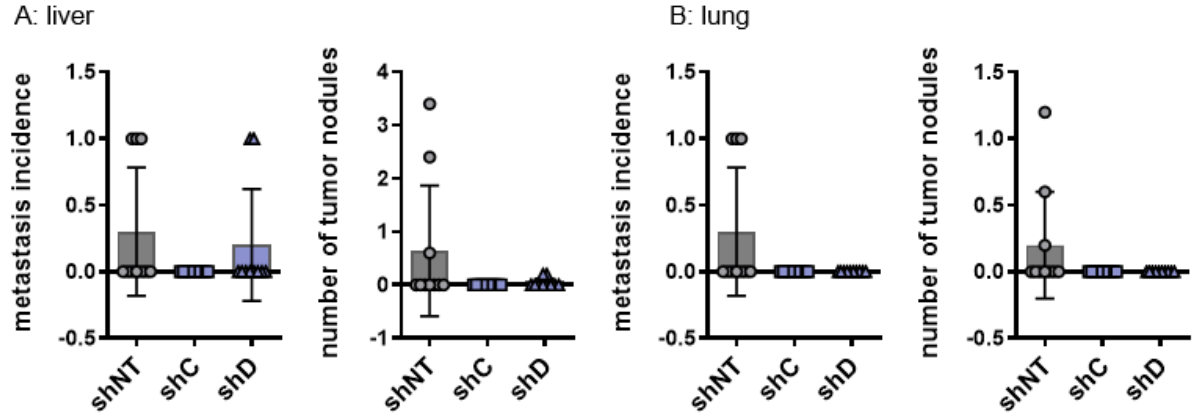

Figure 20: Histological analysis of metastasis to liver and lung from xenograft mouse model after orthotopic injection of NEDD9-competent or -deficient human 786-O cells. A. Incidence of metastasis (left) and number of tumor nodules (right) in the liver. B. Incidence of metastasis (left) and number of tumor nodules (right) in the lung. Statistical evaluation was not possible due to a low metastasis incidence in the NEDD9-deficient groups. shNT, shC, and shD n=10 mice.

In an additional xenograft mouse model, NEDD9-competent (shNT) or -deficient (shC, shD) human 786-O ccRCC cells were injected subcutaneously in the left flank of NSG mice. To assess the aggressiveness of tumor cells in correlation to NEDD9 expression, mitotic figures and giant cells were counted (Fig. 21). Unfortunately, no statistical analysis could be performed because for each of the two NEDD9-deficient groups only one tumor large enough for the assessment of five non-contiguous FOV existed per group. However, the results from the primary tumor development as well as the indicated trend of mitotic figures and giant cells, suggest an impact of NEDD9 on tumor aggressiveness in RCC.

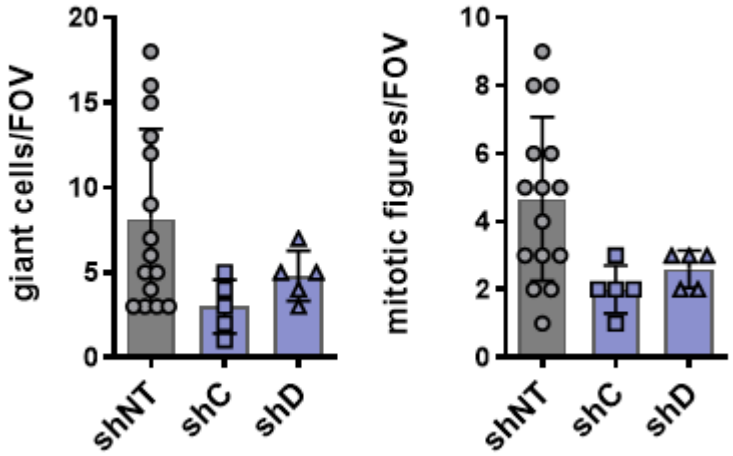

Figure 21: Histological analysis of tumor sections of the xenograft mouse model after subcutaneous injection of NEDD9-competent or -deficient human 786-O cells. Quantification of mitotic figures (left) and giant cells (right) per field of view (FOV). Statistical analysis was not possible due to the low tumor area in the NEDD9-deficient groups. shNT n= 3 mice, shC n=1 mouse, shD n=1 mouse; 5 fields of view per mouse were counted.

5.3 Impact of NEDD9 on the kinome in primary RCC tumors of two different mouse models

To further investigate the underlying pathways of the observed NEDD9 effects, lysates from both the syngeneic and the xenograft orthotopic mouse model were utilized for the analysis of their kinome.

First, lysates from tumor bearing kidneys after orthotopic injection of NEDD9-competent or -deficient murine Renca and human 786-O cells were analyzed for their global kinomic activity using phosphotyrosine kinase (PTK) and serine/threonine kinase (STK) array chips on the PamStation®.

Each array on the chip consists of 144 (STK) or 196 (PTK) peptides that are bound to the porous material of the chip. These peptides are 13 amino acids long and represent phosphorylation sites of specific kinases. During the assay the sample is pumped multiple

times through the chip's pores to enable the kinases in the sample to phosphorylate their respective target peptides in the presence of ATP. After washing away unbound proteins, fluorescently labeled antibodies are added to the sample to visualize the phosphorylation of peptides. By analyzing the phosphorylation pattern of the array and comparing the findings with multiple databases such as Human Protein Reference Database[74,75], Reactome[76], UniProt[77], and Phosphosite[78] it becomes possible to identify the active kinases within the sample.

The kinome assay analysis of NEDD9-deficient tumors derived from the syngeneic mouse model displayed a noticeable reduction in the expression of members belonging to the Src family kinases, particularly c-Src, compared to NEDD9-competent controls (Fig. 22).

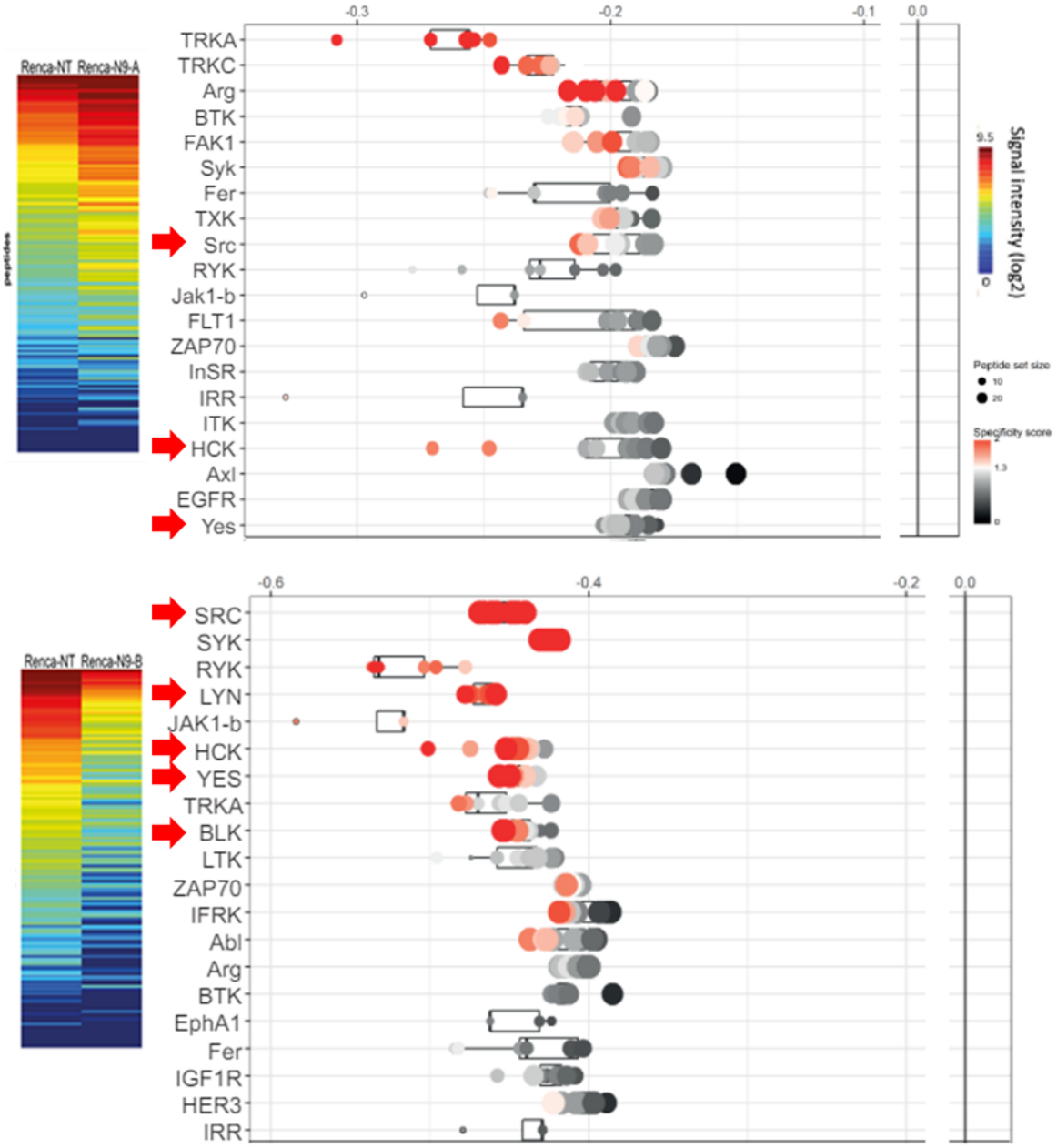

Figure 22: Heat map and upstream kinase activity of protein lysates derived from renal tumors from the syngeneic mouse model after orthotopic injection of NEDD9-competent and -deficient murine Renca cells. Heatmap (left): The Heatmap shows the relation between 2Log-transformed signal intensities and color. Red:

hyperphosphorylation. Blue: hypophosphorylation. Kinase assay (right): Red indicates a high specificity score, i.e. it ranks the kinases based on their significance and specificity in terms of peptides used for the corresponding kinase. Mean kinase statistics are here represented on the horizontal axis and indicate the overall change of the peptide set that represent the kinase when comparing the NEDD9-deficient to the -competent cells. The size of the dot is a representative of the peptide set size of the relative kinase. On the top shNT vs. shA, on the bottom shNT vs. shB. Src kinase family members are marked with a red arrow. n=3.

However, in tumor lysates derived from the xenograft mouse model after orthotopic injection of human 786-O cells a different global kinase activity pattern could be observed. Here Src kinase family appears to be unaffected by NEDD9 expression, whereas the VEGF/FGF pathway was downregulated at low NEDD9 expression levels (Fig. 23).

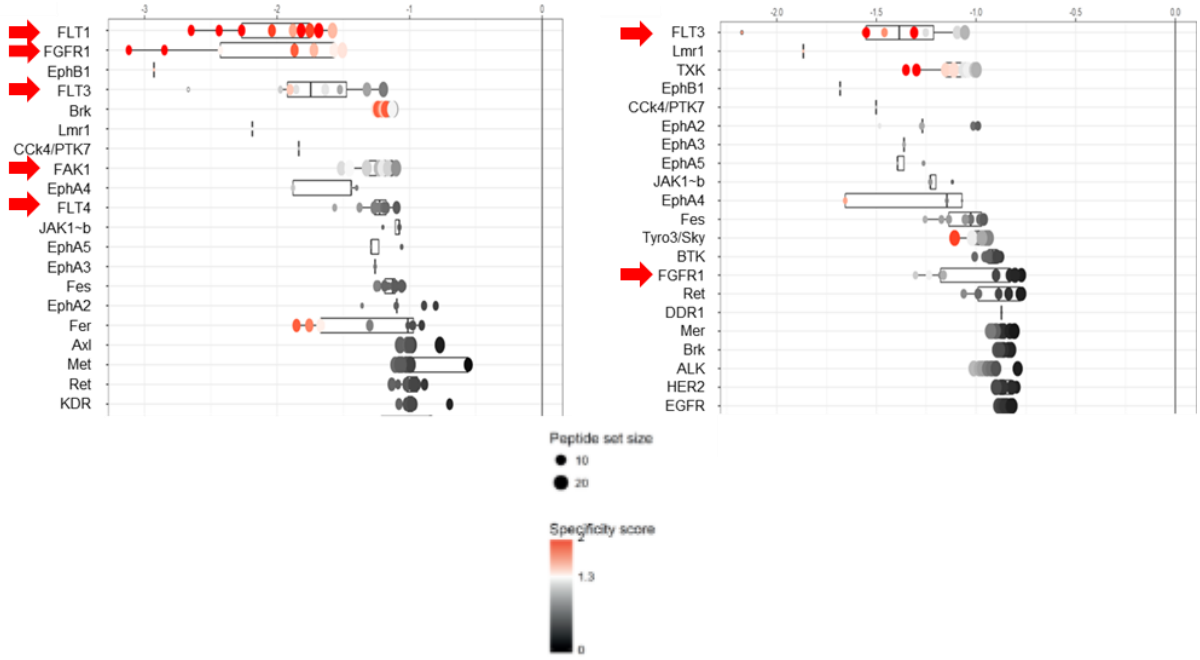

Figure 23: Upstream kinase analysis of protein lysates derived from renal tumors from the xenograft mouse model after orthotopic injection of NEDD9-competent or -deficient human 786-O cells. Red indicates a high specificity score, i.e. it ranks the kinases based on their significance and specificity in terms of peptides used for the corresponding kinase. Mean kinase statistics are here represented on the horizontal axis and indicate the overall change of the peptide set that represent the kinase when comparing the NEDD9-deficient to the -competent cells. The size of the dot is a representative of the peptide set size of the relative kinase. On the left shNT vs. shC, on the right shNT vs. shD. Members of the VEGF/FGF pathway are marked by a red arrow. n=3.

5.4 Effect of NEDD9 expression levels on the transcriptome in 786-O cells via gene microarray

To further elucidate NEDD9-dependent signaling pathways in RCC, RNA microarray for the previously characterized 786-O cells was performed, hence providing an overview of the effect of NEDD9 expression on the tumor cell transcriptome. Databases used for the analysis were: WikiPathway[91], KEGG (Kyoto Encyclopedia of Genes and Genomes) PATHWAY Database[92], Reactome[93] and Gene Ontology[94,95]. These different databases are used to assign the

differently regulated transcripts to specific known pathways or cellular processes. When comparing the datasets obtained from analyzing two groups of NEDD9-deficient cells (sh-C and sh-D) with NEDD9-competent cells, there were 22 genes consistently deregulated in both NEDD9-deficient groups when compared to NEDD9-competent cells. NEDD9-deficient 786-O sh-C cells exhibited deregulation of 79 unique genes compared to NEDD9-competent cells, whereas 786-O sh-D cells showed deregulation of 160 unique genes (Fig. 24).

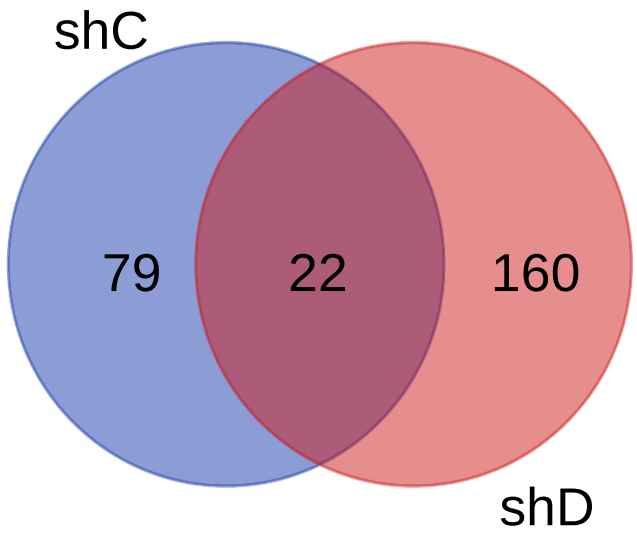

Figure 24: Venn diagram of genes commonly and individually downregulated in 786-O shC and shD cells compared to NEDD9-competent cells.

Transcripts that were commonly downregulated using the beforementioned databases between both NEDD9-deficient groups (786-O sh-C and sh-D) versus NEDD9-competent cells with a p-value ≤0.05 were: MET proto-oncogene (p=0.007), PAK1 (p=0.031), PAK2 (p=0.015), EGFR (p=0.041), PI3K/AKT signaling pathway (p=0.035), ErbB signaling pathway (p=0.038), HIF-1 signaling pathway (p=0.038), transcripts related to type 2 papillary renal cell carcinoma (p=0.007), transcripts related to EGFR tyrosine kinase inhibitor resistance (p=0.035), and HGFR signaling pathway (p=0.016).

Comparing each NEDD9-deficient group individually to NEDD9-competent cells revealed additional differentially regulated transcripts. A comparison of sh-C 786-O cells to NEDD9-competent cells showed the following transcripts and pathways to be significantly downregulated upon low NEDD9 expression levels: ErbB signaling pathway (p=0.005), VEGFA-VEGFR2 signaling pathway (p=0.046), RET signaling (p=0.0001), IRS-mediated signaling (p=0.0002), EGFR (p=0.0005), MAPK1/MAPK3 signaling pathway (p=0.002), PI3K/AKT signaling pathway (p=0.004), PAK1 (p=0.045), PAK2 (p=0.023), and PDGFR signaling pathway (p=0.05).

Transcripts and pathways that are significantly downregulated when comparing NEDD9-deficient sh-D to NEDD-9-competent 786-O cells included: MAP2K and MAPK activation (p=0.011), PI3K/AKT signaling pathway (p=0.028), PAK1 (p=0.006), EGFR (p=0.011), actin filament organization (p=0.026), and MET in type 1 papillary RCC (p=0.027).

In summary, the findings of the previous experiments strongly indicate that NEDD9 has an effect on tumor aggressiveness in ccRCC. This effect seems to be associated with the downregulation of multiple pathways known to modulate tumor aggressiveness (e.g., EGFR pathway, PI3K/AKT signaling and MAPK/ERK pathway).

6. Discussion

As a scaffolding protein, NEDD9 is predicted to have an effect on multiple pathways serving as a central hub where different pathways converge. It is known that NEDD9 is involved in several key functions of tumor growth like migration, invasion and survival[96]. Additionally, elevated NEDD9 expression levels have been shown to predict poor prognosis in many different cancer entities including lung cancer, gastric cancer, breast cancer, ovarian and hepatocellular carcinoma, melanoma and glioblastoma[54,55,65,66,97]. In 2010, Xu et al. were able to show that loss of VHL - the most common genetic aberration in sporadic ccRCCs[11] - leads to high expression levels of NEDD9 through transactivation by HIF-2a and NEDD9-mediated increase in cell motility in ccRCC cells[57]. Later it was demonstrated that NEDD9 is highly expressed in human ccRCC tissue when compared to normal adjacent tissue, as well as in the human ccRCC cell lines 786-O and Caki1[71]. Taken together, these findings indicate a role for NEDD9 in ccRCC disease progression.

In several other tumor entities, like CML, glioblastoma, colorectal cancer and mammary tumors, NEDD9 has been found to interact with different known oncogenic proteins such as FAK, AKT, Src, ERK, BCR-Abl and the Wnt signaling pathway[53,54,62,67,97]. However, except for the upregulation of NEDD9 following VHL inactivation[57], to date, the role of NEDD9 and its interaction partners in tumorigenesis and progression of ccRCC is largely unknown.

The results of the experiments performed here contribute to a better understanding of the role of NEDD9 in ccRCC and the potentially involved signaling pathways and interaction partners.

6.1 NEDD9 depletion leads to a less aggressive tumor phenotype in syngeneic and xenograft RCC mouse models

One major aim of this thesis was to evaluate the effects of NEDD9 expression on RCC *in vivo* by studying histological characteristics from syngeneic and xenograft mouse models injected with ccRCC cells. The presentation of HE slides and the tumor volumes shown on these slides were intended for illustration and further characterization. Quantification of tumor burden was shown in the doctoral thesis of Mariia Cherviakova using MRI imaging and tumor weight[72]. Here, both the syngeneic and the xenograft mouse model show a significant reduction in tumor burden after orthotopic injection of NEDD9-deficient versus – competent Renca or 786-O cells (Fig. 10 and 18). This is in accordance with the findings of Wang et al., where it was shown that in a small cohort of 68 RCC patients a higher tumor stage and shorter overall survival time was significantly associated with higher NEDD9 expression levels. Furthermore, knockdown of NEDD9 in human RCC cells decreased cell migration and invasion *in vitro*[63]. When looking at the phenotype of these tumors and more specifically mitotic figures and giant cells as a marker for a more aggressive tumor growth, renal tumors derived from NEDD9-competent

cells showed significantly more mitotic figures and a tendency to more giant cells compared to tumors consisting of NEDD9-deficient cells in the syngeneic orthotopic model (Fig. 12). This was reflected in the histological analysis of tumors derived from the syngeneic mouse model after subcutaneous injection of NEDD9-competent and -deficient murine Renca cells; here, the number of giant cells as well as mitotic figures showed a significant increase in the NEDD9-competent group when compared to the NEDD9-deficient groups (Fig. 17). Despite the fact that in the xenograft mouse model after subcutaneous injection of NEDD9-competent or -deficient human 786-O cells, statistical analysis was not possible because there was too little tumor tissue in the NEDD9-deficient groups for adequate histological analysis, we notice a visible trend towards more mitotic figures and giant cells in presence of NEDD9 (Fig. 21). A histological analysis of giant cells and mitotic figures in the xenograft mouse model after orthotopic injection was not possible as there was no tumor growth in both NEDD9-deficient groups.

In line with these findings, Pugacheva and Golemis were able to demonstrate that cells overexpressing NEDD9 through interaction with AURKA had multipolar or defective mitotic spindles as well as an irregular number of centrosomes deriving defective cytokinesis[98]. This observation is further reinforced by the results of Dadke et al. where 37-56% of cells with induced NEDD9 expression failed to complete mitosis. In contrast, NEDD9-depleted cells showed problems with the formation of mitotic spindles and cleavage furrows[61], thus suggesting a cell cycle-dependent role for NEDD9. Cell cycle-dependent phosphorylation levels of NEDD9 were previously observed[50] where in early stages of mitosis NEDD9 seems to be supporting the mitotic process, while high NEDD9 expression levels in later stages would hinder cell division[61].

Next, the effect of NEDD9 on the proliferation of renal tumors from the orthotopic syngeneic mouse model was evaluated using Ki67 staining of histological slides. This revealed an increased ratio of Ki67+/Ki67- cells in NEDD9-competent cells in comparison to NEDD9-deficient cells, indicating higher proliferation rates (Fig. 13). In accordance with those results, depletion of NEDD9 has been shown to decrease the number of 786-O cells in the S-phase of mitosis[61] as well as the proliferation of colorectal cancer and melanoma cells[55]. In 2017, a meta-analysis revealed that elevated Ki67 expression levels have been associated with a poor prognosis as well as an advanced disease stage in RCC[99].

Another feature of tumor aggressiveness that was investigated, is the effect of NEDD9 on apoptosis. However, there was no significant difference between NEDD9-competent and -deficient tissue, nor between tumor tissue and normal tissue as caspase 3 levels were generally low. This suggests that NEDD9 has no obvious effects on apoptosis in these models and that tumor growth is not mainly driven by changes in apoptosis (Fig. 14). To date, the effect of NEDD9 on apoptosis is a subject of discussion. In a physiological setting after

induction of apoptosis, NEDD9 is split by caspases developing a C-terminal p28 byproduct; overexpression of this byproduct in MCF-7 breast cancer cells leads to increased apoptosis after initial enhancement of migration. In other cancer entities like glioblastoma and melanoma, NEDD9 overexpression did not lead to an increase in apoptosis[59]. This stands in contrast to Wang et al. where an inhibitory effect of NEDD9 on apoptosis in 786-O cells was suggested[71]. This discrepancy could arise from the different underlying pathways, interactions and other effects of NEDD9 in various cancer entities that remain to be deciphered.

An important aspect when looking at the aggressiveness of a specific tumor is its capacity to metastasize to other organs. When looking at the above-mentioned data, the overall result is inconclusive which could be caused by the limited number of metastases in general in addition to a limited number of histological slides that were available for every investigated organ - namely five per organ - and therefore the whole organ could not be assessed. In the syngeneic mouse model after the orthotopic injection of NEDD9-competent or -deficient murine Renca cells, the metastasis incidence and number of tumor nodules in lung and liver showed no statistical difference (Fig. 15). Likewise, after subcutaneous injection of NEDD9-competent or -deficient murine Renca cells, statistical analysis of metastasis to as well as the number of tumor nodules in kidney and lung was not significant (Fig. 16). Finally, histological analysis of metastasis incidence as well as the number of tumor nodules in the lung and liver of the xenograft mouse model after the orthotopic injection of NEDD9-competent or -deficient human 786-O cells did not allow statistical analysis, because both NEDD9-deficient groups had no metastasis at all and the NEDD9-competent group had very minimal metastasis (Fig. 20). Overall, the results from the different mouse models and injection sites are not conclusive enough to assess an *in vivo* effect of NEDD9 on metastasis. In particular, the models showed a very low metastasizing rate in our hands, so that these models turned out not to be suitable to show a further reduction of metastasis by NEDD9 knockout - as hypothesized. Further models either overexpressing NEDD9 or models with more aggressive metastatic tumors could answer this question in the future.

In line with our hypothesis the findings of Wang et al. showed in a set of human RCC patients, higher TNM-stages connected to higher NEDD9 expression levels[63]. In several other cancer entities like melanoma, colorectal, breast and lung cancer elevated NEDD9 expression levels were shown to be associated with an increased metastatic burden[55,65,67].

Processes on a cellular level that drive metastasis are cell migration or motility and invasion. NEDD9 has been shown to promote migration in colorectal cancer and glioblastoma cells[62,67] as well as to enhance cell motility in a breast cancer cell line[100]. In 2001, van Seventer et al. demonstrated a ß1-integrin/FAK/NEDD9-pathway involved in migration of T- cells and an increased migration upon NEDD9 overexpression[101]. Additionally, NEDD9 has been shown to regulate the GTPase Rac in a complex with DOCK3 and alter the form of cell migration[102].

Another important factor of influence for cell migration is the assembly and disassembly of focal adhesions. Multiple publications have proven an interaction between FAK, one of the most important kinases in focal adhesions and NEDD9[62,67,82,101,103]. O'Neill and Golemis showed focal adhesions, especially their disassembly, to be influenced by cleavage of NEDD9[103]. Crucial for the process of migration and ultimately metastasis is the invasion of tumor cells in surrounding tissue. Fashena et al. were able to show the activation of multiple matrix metalloproteinases and disintegrin, supporting remodeling of the extracellular matrix to facilitate invasion.

In summary, the results here suggest a tumor-promoting role of NEDD99, with expression of NEDD9 being associated with higher tumor cell aggressiveness in RCC models.

6.2 NEDD9 depletion inhibits Src kinases in murine and the VEGF/FGF pathway in human RCC cells

As a scaffolding protein, NEDD9 is predicted to have a multitude of different interaction partners[47]. In a kinome assay of lysates of renal tumors derived from the syngeneic mouse model after orthotopic injection of NEDD9-competent or -deficient murine Renca cells, Src family of kinases and especially Src were some of the top kinases to be downregulated upon decreased NEDD9 levels (Fig. 22). Src was one of the first proto-oncogenes to be discovered and contains four domains: a catalytic, a regulatory and two domains for interactions with other proteins[104]. Src family of kinases consists of nine kinases besides Src: Yrk, Lck, Blk, Lyn, Fyn, Yey, Fgr, and Hck. These kinases have been shown to be involved in B-cell signaling, T cell activation and tumorigenesis[105]. CAS family members and especially NEDD9 have been known to interact with Src kinases: after phosphorylation of the C-terminal binding site, Src family of kinases can bind to NEDD9 via the SH2 domain. The Src kinases in return then phosphorylate NEDD9 creating further binding sites for different downstream effectors[50]. In a breast cancer cell line, Izumchenko et al. were able to demonstrate reduced FAK and Src phosphorylation levels following NEDD9 knockdown[97]. In 2014, Bradbury et al. found that the exchange of NEDD9 at focal adhesions is influenced by SRC activity[60]. Deletion of the NEDD9 domain required for interaction with Src in MEFs resulted in a faster exchange of NEDD9 at focal adhesions[60]. In 2011, Suwaki et al. looked at the role of Src in RCC. They were able to show an association of high Src expression levels with a poor outcome in ccRCC patients.

In a kinome assay of lysates of renal tumors derived from the xenograft mouse model after orthotopic injection of NEDD9-competent or -deficient human 786-O cells, VEGF and other members of the VEGF/FGF pathway were under the top kinases to be downregulated upon low NEDD9 levels (Fig. 23). RCCs and especially ccRCCs are highly vascularized tumors[8] and VEGF inhibitors are to date important players in RCC treatment[42]. In an analysis of activated

RTKs in lysates from human patient-derived ccRCC, VEGFR1 and -2 were significantly phosphorylated in ccRCC tissue when compared to normal adjacent tissue[106]. One of the most common aberrances seen in RCC is the loss of VHL, resulting in an upregulation of HIFs, which in turn induce NEDD9 and positively influence the VEGF[57,107], suggesting a possible interaction between the VEGF pathway and NEDD9 in RCC. In head and neck squamous cell carcinoma cell lines, effects of VEGF on invasion, cell migration and expression of matrix-metalloproteinases was shown to be NEDD9-dependent[108], providing further indications of an interaction.

The observed differences in deregulated pathways between the murine and human cell lines could be due to their genetic background as different species. In mice, VHL loss alone is not able to induce ccRCC development while in human VHL loss represents the most common genetic aberration in ccRCC. This could be caused by differences in the arrangement of genes between the different species. In humans, VHL and other genes most commonly involved in the development of ccRCC are located on chromosome 3p; in mice this group of genes is located on multiple different chromosomes[109].

6.3 NEDD9 deficiency alters expression of multiple known oncogenic pathways in human RCC cells

To examine the effect of altered NEDD9 expression levels on different signaling pathways in human RCC cells, cell lysates of NEDD9-competent and -deficient human 786-O cells were used for a gene microarray. In both NEDD9-deficient groups 22 transcripts were commonly downregulated in comparison to NEDD9-competent cells; 79 transcripts were separately deregulated in sh-C and 160 in sh-D human 786-O cells in comparison to NEDD9-competent cells (Fig. 24). Striking was the downregulation of gene expression of HIF-signaling components in both NEDD9-deficient groups, as VHL mutation and the thereby increased HIF level is the most common mutation in ccRCC[2,10]. In RCC cells, it has been demonstrated that VHL inactivation leads to induction of NEDD9[57]. Additionally, it has been found that the NEDD9 promotor harbors a binding region for HIF-1α[55]. Among the other impacted transcripts were different RTKs, namely EGFR, HGFR, VEGFR2 and PDGFR in addition to their respective pathways. Most of these oncogenic transcripts together with their pathways have already been shown to interact with NEDD9 in different cancer entities, nevertheless never before in RCC. For example the VEGF pathway in head and neck squamous cell cancer was shown to be NEDD9-dependent[108]. In NSCLC cell lines, NEDD9 phosphorylation levels were decreased after inhibition of EGFR[110] and in glioblastoma cells stimulation of PDGFR resulted in elevated NEDD9 phosphorylation levels[62], suggesting NEDD9 to be a downstream effector in both pathways. HGFR also known as MET is an important protein in the pathogenesis of papillary

RCC. The hereditary type of papillary RCC is caused by mutations activating the MET protooncogene and about 13% of sporadic cases have MET mutations[10]. To this date, no direct interaction between NEDD9 and MET has been shown, but it is known that MET is upstream of the NEDD9 interaction partners Src and PI3K[111]. In pancreatic cancer, PI3K and AKT levels were increased after transfection of a NEDD9-pcDNA-vector[112]. Another RTK group member, whose transcripts were downregulated in NEDD9-deficient cells, were ErbB receptors. After induction of NEDD9 in breast cancer cells, ErbB2 receptor levels were elevated in a gene array as well as in Western Blot compared to cells without NEDD9 induction. In the same publication, induction of NEDD9 resulted in raised phosphorylation levels of MAPK, which plays an important role in cell migration[100]. In the assay here, transcripts of MAPK1 and MAPK3 were decreased upon NEDD9-deficiency, indicating an effect of NEDD9 on migration through this interaction. Important for cell migration is the influence of the cytoskeleton with its important component actin. After phosphorylation CAS family proteins contain binding motifs for other proteins. Through a pathway involving Rho family proteins, PAK kinase gets activated, eventually leading to actin remodeling[50,113]. In addition, Kozyreva et al. were able to show an effect of NEDD9 on the regulation of actin dynamics through interaction with CTTN and HDAC6[114].

We have recognized that the number of differentially-expressed overlapping genes in the two NEDD9-deficient cell lines, namely shC and shD, is not as prominent as one should expect. This could be attributed to the fact that here polyclonal cells were utilized. Another reason could be the difference in NEDD9 expression observed after the knockdown transfection as NEDD9 expression in the 786-O shD showed a more dramatic inhibition in comparison to shC. For a further more precise interpretation, monoclonal cells have to be characterized, propagated and further analyzed. Alternatively, a selection vector could be added to the NEDD9-knockdown transfection vector in order to achieve a more stable and cleaner NEDD9-knockdown within the cell line.

In summary, the results in this work indicate that in a xenograft and syngeneic ccRCC mouse model, expression of NEDD9 increases tumor stage as well as tumor cell aggressiveness. Further, indications for the interaction of different oncogenic proteins and signaling pathways like Src, EGFR, VEGF, MET and PI3K/AKT were demonstrated providing additional evidence for NEDD9 as a molecular hub in tumorigenic processes (Fig. 25). Nevertheless, the exact role of NEDD9 in these different interactions needs to be further elucidated to 1. identify new treatment targets important in the pathogenesis of RCC and 2. determine markers for treatment strategy and predictors for treatment response.

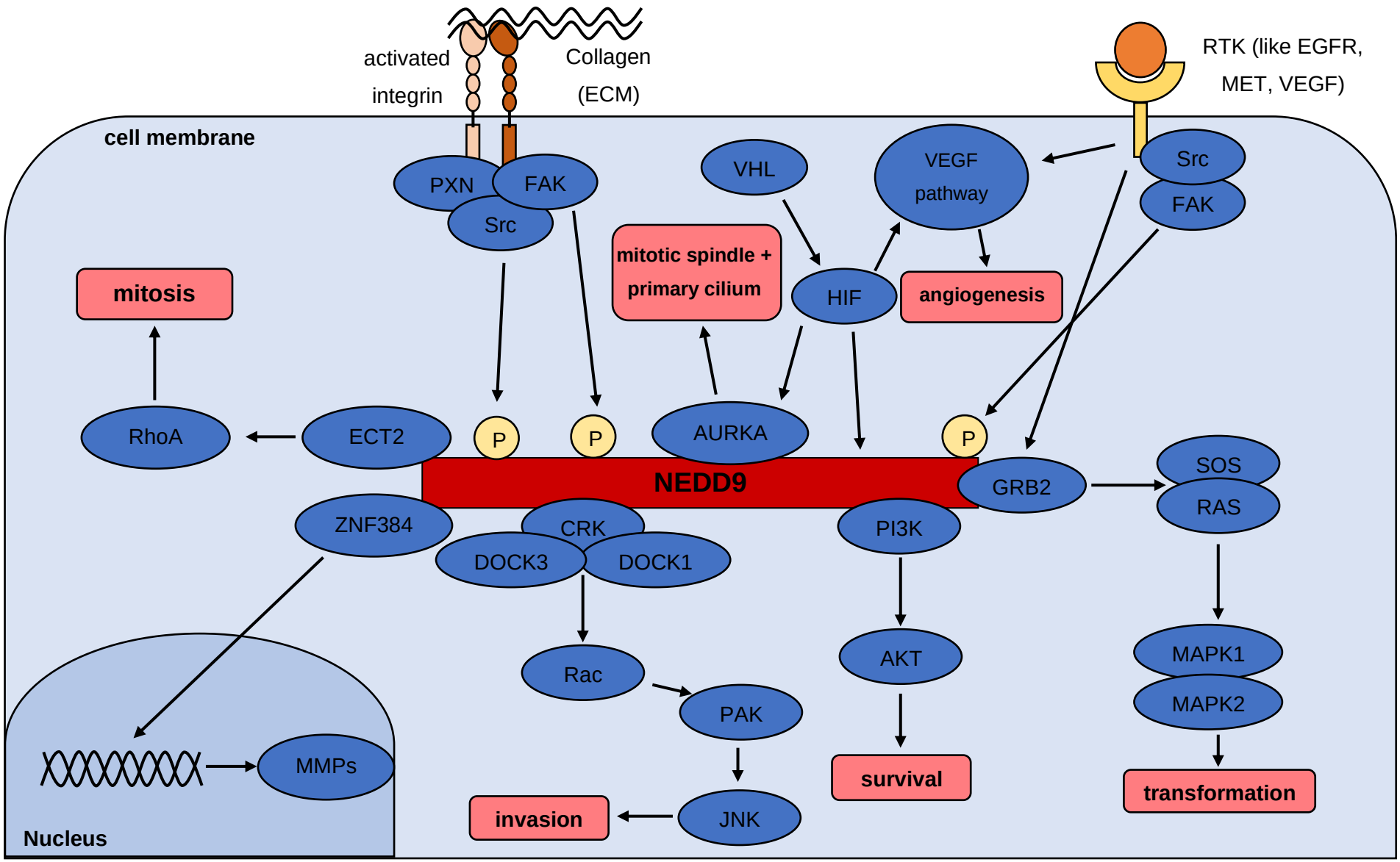

Figure 25: Interactions of the scaffolding protein NEDD9 with other signaling pathways. Adapted and amended from Cabodi et al.[96]

7. Bibliography

1 Sung H, Ferlay J, Siegel RL, *et al.* Global Cancer Statistics 2020: GLOBOCAN Estimates of Incidence and Mortality Worldwide for 36 Cancers in 185 Countries. *CA Cancer J Clin* 2021; **71**: 209–49.

2 Petejova N, Martinek A. Renal cell carcinoma: Review of etiology, pathophysiology and risk factors. *Biomed Pap Med Fac Univ Palacky Olomouc Czech Repub* 2016; **160**: 183–94.

3 Capitanio U, Bensalah K, Bex A, *et al.* Epidemiology of Renal Cell Carcinoma. *European Urology* 2019; **75**: 74–84.

4 Ferlay J, Laversanne M, Ervik M, *et al.* Global Cancer Observatory: Cancer Tomorrow. https://gco.iarc.fr/tomorrow (accessed Aug 16, 2023).

5 Vasudev NS, Wilson M, Stewart GD, *et al.* Challenges of early renal cancer detection: symptom patterns and incidental diagnosis rate in a multicentre prospective UK cohort of patients presenting with suspected renal cancer. *BMJ Open* 2020; **10**: e035938.

6 Escudier B, Porta C, Schmidinger M, *et al.* Renal cell carcinoma: ESMO Clinical Practice Guidelines for diagnosis, treatment and follow-up†. *Annals of Oncology* 2019; **30**: 706–20.

7 Motzer RJ, Jonasch E, Boyle S, *et al.* NCCN Guidelines Insights: Kidney Cancer, Version 1.2021: Featured Updates to the NCCN Guidelines. *Journal of the National Comprehensive Cancer Network* 2020; **18**: 1160–70.

8 Prasad SR, Humphrey PA, Catena JR, *et al.* Common and Uncommon Histologic Subtypes of Renal Cell Carcinoma: Imaging Spectrum with Pathologic Correlation. *RadioGraphics* 2006; **26**: 1795–806.

9 Choueiri TK, Kaelin WG. Targeting the HIF2–VEGF axis in renal cell carcinoma. *Nat Med* 2020; **26**: 1519–30.

10 Adeniran AJ, Shuch B, Humphrey PA. Hereditary Renal Cell Carcinoma Syndromes: Clinical, Pathologic, and Genetic Features. *Am J Surg Pathol* 2015; **39**: e1–18.

11 Li L, Kaelin WG. New insights into the biology of renal cell carcinoma. *Hematol Oncol Clin North Am* 2011; **25**: 667–86.

12 Mitchell TJ, Turajlic S, Rowan A, *et al.* Timing the Landmark Events in the Evolution of Clear Cell Renal Cell Cancer: TRACERx Renal. *Cell* 2018; **173**: 611-623.e17.

13 Jonasch E, Gao J, Rathmell WK. Renal cell carcinoma. *BMJ* 2014; **349**: g4797.

14 Dunnick NR. Renal cell carcinoma: staging and surveillance. *Abdom Radiol (NY)* 2016; **41**: 1079–85.

15 Rankin EB, Tomaszewski JE, Haase VH. Renal Cyst Development in Mice with Conditional Inactivation of the von Hippel-Lindau Tumor Suppressor. *Cancer Res* 2006; **66**: 2576–83.

16 Jonasch E, Walker CL, Rathmell WK. Clear cell renal cell carcinoma ontogeny and mechanisms of lethality. *Nat Rev Nephrol* 2021; **17**: 245–61.

17 Sanfrancesco JM, Cheng L. Complexity of the genomic landscape of renal cell carcinoma: Implications for targeted therapy and precision immuno-oncology. *Crit Rev Oncol Hematol* 2017; **119**: 23–8.

18 Padala SA, Barsouk A, Thandra KC, *et al.* Epidemiology of Renal Cell Carcinoma. *World J Oncol* 2020; **11**: 79–87.

19 Ljungberg B, Albiges L, Abu-Ghanem Y, *et al.* European Association of Urology Guidelines on Renal Cell Carcinoma: The 2022 Update. *European Urology* 2022; **82**: 399–410.

20 Jian Y, Yang K, Sun X, *et al.* Current Advance of Immune Evasion Mechanisms and Emerging Immunotherapies in Renal Cell Carcinoma. *Front Immunol* 2021; **12**: 639636.

21 Brierley JD, Gospodarowicz MK, Wittekind C, editors. TNM Classification of Malignant Tumours, 8th Edition, 8th edn. New York: John Wiley & Sons, 2017 https://www.wiley.com/en-us/TNM+Classification+of+Malignant+Tumours%2C+8th+Edition-p-9781119263562 (accessed Sept 15, 2020).

22 Bianchi M, Sun M, Jeldres C, *et al.* Distribution of metastatic sites in renal cell carcinoma: a population-based analysis. *Annals of Oncology* 2012; **23**: 973–80.

23 Elmore JM, Kadesky KT, Koeneman KS, Sagalowsky AI. Reassessment of the 1997 TNM classification system for renal cell carcinoma. *Cancer* 2003; **98**: 2329–34.

24 Amin MB, Edge S, Greene F, *et al.*, editors. AJCC Cancer Staging Manual, 8th edn. Springer International Publishing, 2017 https://www.springer.com/us/book/9783319406176 (accessed Sept 15, 2020).

25 MacLennan S, Imamura M, Lapitan MC, *et al.* Systematic Review of Oncological Outcomes Following Surgical Management of Localised Renal Cancer. *European Urology* 2012; **61**: 972–93.

26 Buti S, Bersanelli M, Sikokis A, *et al.* Chemotherapy in metastatic renal cell carcinoma today? A systematic review. *Anticancer Drugs* 2013; **24**: 535–54.

27 Makhov P, Joshi S, Ghatalia P, Kutikov A, Uzzo RG, Kolenko VM. Resistance to Systemic Therapies in Clear Cell Renal Cell Carcinoma: Mechanisms and Management Strategies. *Molecular Cancer Therapeutics* 2018; **17**: 1355–64.

28 Sharma R, Kadife E, Myers M, Kannourakis G, Prithviraj P, Ahmed N. Determinants of resistance to VEGF-TKI and immune checkpoint inhibitors in metastatic renal cell carcinoma. *J Exp Clin Cancer Res* 2021; **40**: 186.

29 Srinivasan R, Ricketts CJ, Sourbier C, Linehan WM. New strategies in renal cell carcinoma: targeting the genetic and metabolic basis of disease. *Clin Cancer Res* 2015; **21**: 10–7.

30 Zarrabi K, Fang C, Wu S. New treatment options for metastatic renal cell carcinoma with prior anti-angiogenesis therapy. *J Hematol Oncol* 2017; **10**: 38.

31 Ljungberg B, Albiges L, Abu-Ghanem Y, *et al.* European Association of Urology Guidelines on Renal Cell Carcinoma: The 2022 Update. *European Urology* 2022; **82**: 399–410.

32 Mendiratta P, Rini BI, Ornstein MC. Emerging immunotherapy in advanced renal cell carcinoma. *Urologic Oncology: Seminars and Original Investigations* 2017; **35**: 687–93.

33 McKay RR, Bossé D, Choueiri TK. Evolving Systemic Treatment Landscape for Patients With Advanced Renal Cell Carcinoma. *JCO* 2018; **36**: 3615–23.

34 Hanahan D, Weinberg RA. Hallmarks of Cancer: The Next Generation. *Cell* 2011; **144**: 646–74.

35 Ribas A, Wolchok JD. Cancer Immunotherapy Using Checkpoint Blockade. *Science* 2018; **359**: 1350–5.

36 Motzer RJ, Tannir NM, McDermott DF, *et al.* Nivolumab plus Ipilimumab versus Sunitinib in Advanced Renal-Cell Carcinoma. *New England Journal of Medicine* 2018; **378**: 1277–90.

37 Motzer R, Alekseev B, Rha S-Y, *et al.* Lenvatinib plus Pembrolizumab or Everolimus for Advanced Renal Cell Carcinoma. *N Engl J Med* 2021; **384**: 1289–300.

38 Choueiri TK, Powles T, Burotto M, *et al.* Nivolumab plus Cabozantinib versus Sunitinib for Advanced Renal-Cell Carcinoma. *N Engl J Med* 2021; **384**: 829–41.

39 Motzer RJ, Penkov K, Haanen J, *et al.* Avelumab plus Axitinib versus Sunitinib for Advanced Renal-Cell Carcinoma. *N Engl J Med* 2019; **380**: 1103–15.

40 Tenold M, Ravi P, Kumar M, *et al.* Current Approaches to the Treatment of Advanced or Metastatic Renal Cell Carcinoma. *American Society of Clinical Oncology Educational Book* 2020; : 187–96.

41 Heng DYC, Xie W, Regan MM, *et al.* Prognostic Factors for Overall Survival in Patients With Metastatic Renal Cell Carcinoma Treated With Vascular Endothelial Growth Factor–Targeted Agents: Results From a Large, Multicenter Study. *JCO* 2009; **27**: 5794–9.

42 Leitlinienprogramm Onkologie. Diagnostik, Therapie und Nachsorge des Nierenzellkarzinoms, Langversion 3.0. 2021. https://www.leitlinienprogramm-onkologie.de/leitlinien/nierenzellkarzinom/ (accessed March 20, 2022).

43 Rini BI, Plimack ER, Stus V, *et al.* Pembrolizumab plus Axitinib versus Sunitinib for Advanced Renal-Cell Carcinoma. *N Engl J Med* 2019; **380**: 1116–27.

44 Pal SK, Puente J, Heng DYC, *et al.* Assessing the Safety and Efficacy of Two Starting Doses of Lenvatinib Plus Everolimus in Patients with Renal Cell Carcinoma: A Randomized Phase 2 Trial. *European Urology* 2022; **82**: 283–92.

45 Sepe P, Mennitto A, Corti F, Procopio G. Immunotherapeutic Targets and Therapy for Renal Cell Carcinoma. *Immunotargets Ther* 2020; **9**: 273–88.

46 Rassy E, Flippot R, Albiges L. Tyrosine kinase inhibitors and immunotherapy combinations in renal cell carcinoma. *Ther Adv Med Oncol* 2020; **12**: 1758835920907504.

47 Shaw AS, Filbert EL. Scaffold proteins and immune-cell signalling. *Nature Reviews Immunology* 2009; **9**: 47–56.

48 DiRusso CJ, Dashtiahangar M, Gilmore TD. Scaffold proteins as dynamic integrators of biological processes. *J Biol Chem* 2022; **298**: 102628.

49 Good MC, Zalatan JG, Lim WA. Scaffold Proteins: Hubs for Controlling the Flow of Cellular Information. *Science* 2011; **332**: 680–6.

50 Tikhmyanova N, Little JL, Golemis EA. CAS proteins in normal and pathological cell growth control. *Cell Mol Life Sci* 2010; **67**: 1025–48.

51 Law SF, Zhang Y-Z, Fashena SJ, Toby G, Estojak J, Golemis EA. Dimerization of the Docking/Adaptor Protein HEF1 via a Carboxy-Terminal Helix-Loop-Helix Domain. *Experimental Cell Research* 1999; **252**: 224–35.

52 Arold ST, Hoellerer MK, Noble MEM. The Structural Basis of Localization and Signaling by the Focal Adhesion Targeting Domain. *Structure* 2002; **10**: 319–27.

53 Hu Z, Wei F, Su Y, *et al.* Histone deacetylase inhibitors promote breast cancer metastasis by elevating NEDD9 expression. *Signal Transduct Target Ther* 2023; **8**: 11.

54 Nikonova AS, Gaponova AV, Kudinov AE, Golemis EA. CAS proteins in health and disease: an update. *IUBMB Life* 2014; **66**: 387–95.

55 Shagisultanova E, Gaponova AV, Gabbasov R, Nicolas E, Golemis EA. Preclinical and clinical studies of the NEDD9 scaffold protein in cancer and other diseases. *Gene* 2015; **567**: 1–11.

56 Lu R, Ji Z, Li X, *et al.* miR-145 functions as tumor suppressor and targets two oncogenes, ANGPT2 and NEDD9, in renal cell carcinoma. *J Cancer Res Clin Oncol* 2014; **140**: 387–97.

57 Xu J, Li H, Wang B, *et al.* VHL inactivation induces HEF1 and Aurora kinase A. *J Am Soc Nephrol* 2010; **21**: 2041–6.

58 Law SF, Zhang YZ, Klein-Szanto AJ, Golemis EA. Cell cycle-regulated processing of HEF1 to multiple protein forms differentially targeted to multiple subcellular compartments. *Mol Cell Biol* 1998; **18**: 3540–51.

59 Singh MK, Cowell L, Seo S, O'Neill GM, Golemis EA. Molecular basis for HEF1/NEDD9/Cas-L action as a multifunctional coordinator of invasion, apoptosis and cell cycle. *Cell Biochem Biophys* 2007; **48**: 54–72.

60 Bradbury P, Bach CT, Paul A, O'Neill GM. Src Kinase Determines the Dynamic Exchange of the Docking Protein NEDD9 (Neural Precursor Cell Expressed Developmentally Down-regulated Gene 9) at Focal Adhesions. *J Biol Chem* 2014; **289**: 24792–800.

61 Dadke D, Jarnik M, Pugacheva EN, Singh MK, Golemis EA. Deregulation of HEF1 impairs M-phase progression by disrupting the RhoA activation cycle. *Mol Biol Cell* 2006; **17**: 1204–17.

62 Natarajan M, Stewart JE, Golemis EA, *et al.* HEF1 is a necessary and specific downstream effector of FAK that promotes the migration of glioblastoma cells. *Oncogene* 2006; **25**: 1721–32.

63 Wang J, Wang S, Luan Y, *et al.* Overexpression of NEDD9 in renal cell carcinoma is associated with tumor migration and invasion. *Oncol Lett* 2017; **14**: 8021–7.

64 Rusyn L, Reinartz S, Nikiforov A, *et al.* The scaffold protein NEDD9 is necessary for leukemia-cell migration and disease progression in a mouse model of chronic lymphocytic leukemia. *Leukemia* 2022; **36**: 1794–805.

65 Gabbasov R, Xiao F, Howe CG, *et al.* NEDD9 promotes oncogenic signaling, a stem/mesenchymal gene signature, and aggressive ovarian cancer growth in mice. *Oncogene* 2018; **37**: 4854–70.

66 Gu Y, Lu J, Chen C, Zheng F. NEDD9 overexpression predicts poor prognosis in solid cancers: a meta-analysis. *Onco Targets Ther* 2019; **12**: 4213–22.

67 Li Y, Bavarva JH, Wang Z, *et al.* HEF1, a novel target of Wnt signaling, promotes colonic cell migration and cancer progression. *Oncogene* 2011; **30**: 2633–43.

68 Deneka AY, Kopp MC, Nikonova AS, *et al.* Nedd9 restrains autophagy to limit growth of early stage non-small cell lung cancer. *Cancer Res* 2021; **81**: 3717–26.

69 Beck TN, Nicolas E, Kopp MC, Golemis EA. Adaptors for disorders of the brain? The cancer signaling proteins NEDD9, CASS4, and PTK2B in Alzheimer's disease. *Oncoscience* 2014; **1**: 486–503.

70 Nikonova AS, Plotnikova OV, Serzhanova V, *et al.* Nedd9 restrains renal cystogenesis in Pkd1-/- mice. *Proc Natl Acad Sci USA* 2014; **111**: 12859–64.

71 Wang J, Yang W-J, Sun C, *et al.* siRNA Suppression of NEDD9 Inhibits Proliferation and Enhances Apoptosis in Renal Cell Carcinoma. *Oncol Res* 2014; **22**: 219–24.

72 Cherviakova M. Die Rolle von NEDD9 in der Pathogenese des klarzelligen Nierenzellkarzinoms. 2021.

73 Carlotti F, Bazuine M, Kekarainen T, *et al.* Lentiviral Vectors Efficiently Transduce Quiescent Mature 3T3-L1 Adipocytes. *Molecular Therapy* 2004; **9**: 209–17.

74 Peri S, Navarro JD, Amanchy R, *et al.* Development of human protein reference database as an initial platform for approaching systems biology in humans. *Genome Res* 2003; **13**: 2363–71.

75 Keshava Prasad TS, Goel R, Kandasamy K, *et al.* Human Protein Reference Database--2009 update. *Nucleic Acids Res* 2009; **37**: D767-772.

76 Gillespie M, Jassal B, Stephan R, *et al.* The reactome pathway knowledgebase 2022. *Nucleic Acids Research* 2022; **50**: D687–92.

77 The UniProt Consortium. UniProt: the Universal Protein Knowledgebase in 2023. *Nucleic Acids Research* 2023; **51**: D523–31.

78 Hornbeck PV, Zhang B, Murray B, Kornhauser JM, Latham V, Skrzypek E. PhosphoSitePlus, 2014: mutations, PTMs and recalibrations. *Nucleic Acids Res* 2015; **43**: D512-520.

79 Sherman BT, Hao M, Qiu J, *et al.* DAVID: a web server for functional enrichment analysis and functional annotation of gene lists (2021 update). *Nucleic Acids Res* 2022; **50**: W216–21.

80 Huang DW, Sherman BT, Lempicki RA. Systematic and integrative analysis of large gene lists using DAVID bioinformatics resources. *Nat Protoc* 2009; **4**: 44–57.

81 Cahan P, Li H, Morris SA, Lummertz da Rocha E, Daley GQ, Collins JJ. CellNet: Network Biology Applied to Stem Cell Engineering. *Cell* 2014; **158**: 903–15.

82 Law SF, Estojak J, Wang B, Mysliwiec T, Kruh G, Golemis EA. Human enhancer of filamentation 1, a novel p130cas-like docking protein, associates with focal adhesion kinase and induces pseudohyphal growth in Saccharomyces cerevisiae. *Mol Cell Biol* 1996; **16**: 3327–37.

83 Potter H, Heller R. Transfection by Electroporation. *Curr Protoc Mol Biol* 2018; **121**: 9.3.1-9.3.13.

84 Kumar V, Abbas AK, Fausto N. Robbins & Cotran Pathologic Basis of Disease, 7th edn. W B Saunders Co Ltd, 2004.

85 Mirzayans R, Andrais B, Murray D. Roles of Polyploid/Multinucleated Giant Cancer Cells in Metastasis and Disease Relapse Following Anticancer Treatment. *Cancers (Basel)* 2018; **10**: 118.

86 Williamson SR, Kum JB, Goheen MP, Cheng L, Grignon DJ, Idrees MT. Clear cell renal cell carcinoma with a syncytial-type multinucleated giant tumor cell component: implications for differential diagnosis. *Human Pathology* 2014; **45**: 735–44.

87 Gerdes J, Lemke H, Baisch H, Wacker HH, Schwab U, Stein H. Cell cycle analysis of a cell proliferation-associated human nuclear antigen defined by the monoclonal antibody Ki-67. *The Journal of Immunology* 1984; **133**: 1710–5.

88 Asadi M, Taghizadeh S, Kaviani E, *et al.* Caspase-3: Structure, function, and biotechnological aspects. *Biotechnol Appl Biochem* 2022; **69**: 1633–45.

89 Harrington HA, Ho KL, Ghosh S, Tung K. Construction and analysis of a modular model of caspase activation in apoptosis. *Theoretical Biology and Medical Modelling* 2008; **5**: 26.

90 Hanahan D, Weinberg RA. The Hallmarks of Cancer. *Cell* 2000; **100**: 57–70.

91 Martens M, Ammar A, Riutta A, *et al.* WikiPathways: connecting communities. *Nucleic Acids Research* 2021; **49**: D613–21.

92 Kanehisa M, Goto S. KEGG: Kyoto Encyclopedia of Genes and Genomes. *Nucleic Acids Res* 2000; **28**: 27–30.

93 Jassal B, Matthews L, Viteri G, *et al.* The reactome pathway knowledgebase. *Nucleic Acids Res* 2020; **48**: D498–503.

94 Ashburner M, Ball CA, Blake JA, *et al.* Gene Ontology: tool for the unification of biology. *Nat Genet* 2000; **25**: 25–9.

95 The Gene Ontology Consortium. The Gene Ontology resource: enriching a GOld mine. *Nucleic Acids Research* 2021; **49**: D325–34.

96 Cabodi S, del Pilar Camacho-Leal M, Di Stefano P, Defilippi P. Integrin signalling adaptors: not only figurants in the cancer story. *Nat Rev Cancer* 2010; **10**: 858–70.

97 Izumchenko E, Singh MK, Plotnikova OV, *et al.* NEDD9 promotes oncogenic signaling in mammary tumor development. *Cancer Res* 2009; **69**: 7198–206.

98 Pugacheva EN, Golemis EA. The focal adhesion scaffolding protein HEF1 regulates activation of the Aurora-A and Nek2 kinases at the centrosome. *Nat Cell Biol* 2005; **7**: 937–46.

99 Xie Y, Chen L, Ma X, *et al.* Prognostic and clinicopathological role of high Ki-67 expression in patients with renal cell carcinoma: a systematic review and meta-analysis. *Sci Rep* 2017; **7**: 44281.

100 Fashena SJ, Einarson MB, O'Neill GM, Patriotis C, Golemis EA. Dissection of HEF1-dependent functions in motility and transcriptional regulation. *Journal of Cell Science* 2002; **115**: 99–111.

101 van Seventer GA, Salmen HJ, Law SF, *et al.* Focal adhesion kinase regulates beta1 integrin-dependent T cell migration through an HEF1 effector pathway. *Eur J Immunol* 2001; **31**: 1417–27.

102 Sanz-Moreno V, Gadea G, Ahn J, *et al.* Rac Activation and Inactivation Control Plasticity of Tumor Cell Movement. *Cell* 2008; **135**: 510–23.

103 O'Neill GM, Golemis EA. Proteolysis of the Docking Protein HEF1 and Implications for Focal Adhesion Dynamics. *Molecular and Cellular Biology* 2001; **21**: 5094–108.

104 Martin GS. The hunting of the Src. *Nat Rev Mol Cell Biol* 2001; **2**: 467–75.

105 Parsons SJ, Parsons JT. Src family kinases, key regulators of signal transduction. *Oncogene* 2004; **23**: 7906–9.

106 Zhang Q, Liu J-H, Liu J-L, *et al.* Activation and function of receptor tyrosine kinases in human clear cell renal cell carcinomas. *BMC Cancer* 2019; **19**: 1044.

107 Cross MJ, Claesson-Welsh L. FGF and VEGF function in angiogenesis: signalling pathways, biological responses and therapeutic inhibition. *Trends in Pharmacological Sciences* 2001; **22**: 201–7.

108 Lucas JT, Salimath BP, Slomiany MG, Rosenzweig SA. Regulation of Invasive Behavior by Vascular Endothelial Growth Factor is HEF1-dependent. *Oncogene* 2010; **29**: 4449–59.

109 Wolf MM, Rathmell WK, Beckermann KE. Modeling Clear Cell Renal Cell Carcinoma and Therapeutic Implications. *Oncogene* 2020; **39**: 3413–26.

110 Kondo S, Iwata S, Yamada T, *et al.* Impact of the Integrin Signaling Adaptor Protein NEDD9 on Prognosis and Metastatic Behavior of Human Lung Cancer. *Clinical Cancer Research* 2012; **18**: 6326–38.

111 Organ SL, Tsao M-S. An overview of the c-MET signaling pathway. *Ther Adv Med Oncol* 2011; **3**: S7–19.

112 Xue Y, Zhong Y, Wu T, *et al.* Anti-Proliferative and Apoptosis-Promoting Effect of microRNA-125b on Pancreatic Cancer by Targeting NEDD9 via PI3K/AKT Signaling. *Cancer Manag Res* 2020; **12**: 7363–73.

113 Ridley AJ. Rho GTPases and cell migration. *Journal of Cell Science* 2001; **114**: 2713–22.

114 Kozyreva VK, McLaughlin SL, Livengood RH, *et al.* NEDD9 regulates actin dynamics through cortactin deacetylation in an AURKA/HDAC6-dependent manner. *Mol Cancer Res* 2014; **12**: 681–93.

8. Appendix

8.1 List of figures

8.2 List of Tables